

1 **Non-Hydrostatic RegCM4 (RegCM4-NH): Model description**  
2 **and case studies over multiple domains.**

3 Coppola Erika (1), Stocchi Paolo (2), Pichelli Emanuela (1), Torres Alavez Jose Abraham  
4 (1), Glazer Russel (1), Giuliani Graziano (1), Di Sante Fabio (1), Nogherotto Rita (1), Giorgi  
5 Filippo (1)

6 *Correspondence to:* Erika Coppola ([coppolae@ictp.it](mailto:coppolae@ictp.it))

7 1. International Centre for Theoretical Physics (ICTP), Trieste, Italy  
8 2. Institute of Atmospheric Sciences and Climate, National Research Council of Italy, CNR-ISAC,  
9 Bologna, Italy

10 **Abstract**

11 We describe the development of a non-hydrostatic version of the regional climate model  
12 RegCM4, called RegCM4-NH, for use at convection-permitting resolutions. The non-  
13 hydrostatic dynamical core of the Mesoscale Model MM5 is introduced in the RegCM4,  
14 with some modifications to increase stability and applicability of the model to long-term  
15 climate simulations. Newly available explicit microphysics schemes are also described,  
16 and three case studies of intense convection events are carried out in order to illustrate  
17 the performance of the model. They are all run at convection-permitting grid spacing of 3  
18 km over domains in northern California, Texas and the Lake Victoria region, without the  
19 use of parameterized cumulus convection. A substantial improvement is found in several  
20 aspects of the simulations compared to corresponding coarser resolution (12 km) runs  
21 completed with the hydrostatic version of the model employing parameterized convection.  
22 RegCM4-NH is currently being used in different projects for regional climate simulations  
23 at convection-permitting resolutions, and is intended to be a resource for users of the  
24 RegCM modeling system.

25

26 **Keywords:**

27 Regional climate models; RegCM4; km-scale resolution; climate change

28 **Introduction**

29 Since the pioneering work of Dickinson et al. (1989) and Giorgi and Bates (1989),  
30 documenting the first regional climate modeling system (RegCM, version 1) in literature,  
31 the dynamical downscaling technique based on limited area Regional Climate Models  
32 (RCMs) has been widely used worldwide, and a number of RCM systems have been  
33 developed (Giorgi 2019). RegCM1 (Dickinson et al., 1989, Giorgi and Bates, 1989) was  
34 originally developed at the National Center for Atmospheric Research (NCAR) based on  
35 the Mesoscale Model version 4 (MM4) (Anthes et al, 1987) . Then, further model versions  
36 followed: RegCM2 (Giorgi et al. 1993a,b), RegCM2.5, (Giorgi and Mearns 1999),  
37 RegCM3 (Pal et al. 2007), and lastly RegCM4 (Giorgi et al 2012). Except for the transition  
38 from RegCM1 to RegCM2, in which the model dynamical core was updated from that of  
39 the MM4 to that of the MM5 (Grell et al. 1995), these model evolutions were mostly based  
40 on additions of new and more advanced physics packages. RegCM4 is today used by a  
41 large community for numerous projects and applications, from process studies to paleo  
42 and future climate projections, including participation in the Coordinated Regional  
43 Downscaling EXperiment (CORDEX, Giorgi et al. 2009; Gutowski et al. 2016). The model  
44 can also be coupled with ocean, land and chemistry/aerosol modules in a fully interactive  
45 way (Sitz et al. 2017).

46 The dynamical core of the standard version of RegCM4 is hydrostatic, with sigma-p  
47 vertical coordinates. As a result, the model can be effectively run for grid spacings of ~10  
48 km or larger, for which the hydrostatic assumption is valid. However, the RCM community  
49 is rapidly moving to higher resolutions of a few km, i.e. “convection-permitting” (Prein et  
50 al. 2015; Coppola et al. 2020) and therefore the dynamical core of RegCM4 has been  
51 upgraded to include a non-hydrostatic dynamics representation usable for very high  
52 resolution applications. This upgrade, which we name RegCM4-NH, is essentially based  
53 on the implementation of the MM5 non-hydrostatic dynamical core within the RegCM4  
54 framework, which has an entirely different set of model physics compared to MM5.

55

56 RegCM4-NH is already being used in some international projects focusing on climate  
57 simulations at convection-permitting km-scales, namely the European Climate Prediction  
58 System (EUCP, Hewitt and Lowe 2018) and the CORDEX Flagship Pilot Study dedicated

59 to convection (CORDEX-FPSCONV, Coppola et al. 2020), and it is starting to be used  
60 more broadly by the RegCM modeling community.

61 For example, the recent papers by Ban et al. (2021) and Pichelli et al. (2021) document  
62 results of the first multi-model experiment of 10-year simulations at the convection-  
63 permitting scales over the so-called greater Alpine region. Two different simulations with  
64 RegCM4-NH for present day conditions have contributed to the evaluation analysis of  
65 Ban et al. (2021). They were carried out at the International Centre for Theoretical Physics  
66 (ICTP) and the Croatian Meteorological and Hydrological Service (DHMZ) using two  
67 different physics configurations. The results show that RegCM4-NH largely improves the  
68 precipitation simulation as compared to available fine scale observations when going from  
69 coarse to high resolution, in particular for higher order statistics, such as precipitation  
70 extremes and hourly intensity. Pichelli et al. (2021) then analyse multi-model ensemble  
71 simulations driven by selected CMIP5 GCM projections for the decades 1996–2005 and  
72 2090–2099 under the RCP8.5 scenario. ICTP contributed to the experiment with  
73 simulations using RegCM4-NH driven by the MOCH-HadGEM GCM (r1i1p1) in a two  
74 level nest configuration (respectively at 12 and 3 km grid). The paper shows new insights  
75 into future changes, for example an enhancement of summer and autumn hourly rainfall  
76 intensification compared to coarser resolution model experiments, as well as an increase  
77 of frequency and intensity of high-impact weather events.

78

79 In this paper we describe the structure of RegCM4-NH and provide some illustrative  
80 examples of its performance, so that model users can have a basic reference providing  
81 them with background information on the model. In the next section we first describe the  
82 new model dynamical core, while the illustrative applications are presented in section 4.  
83 Section 5 finally provides some discussion of future developments planned for the RegCM  
84 system.

85 **Model description**

86 In the development of RegCM4-NH, the RegCM4 as described by Giorgi et al. (2012) was  
87 modified to include, the non-hydrostatic dynamical core (*idynamic* = 2 namelist option as  
88 described in RegCM-4.7.1/Doc/README.namelist of the source code) of the mesoscale

89 model MM5 (Grell et al. 1995). This dynamical core was selected because RegCM4  
90 already has the same grid and variable structure as MM5 in its hydrostatic core, which  
91 substantially facilitated its implementation (Elguindi et al. 2017).

92

93 The model equations with complete description of the Coriolis force and a top radiative  
94 boundary condition, along with the finite differencing scheme, are given in Grell et al.  
95 (1995). Pressure,  $p$ , temperature,  $T$ , and density,  $\rho$ , are first decomposed into a  
96 prescribed reference vertical profile plus a time varying perturbation. The prognostic  
97 equations are then calculated using the pressure perturbation values. Compared to the  
98 original MM5 dynamical core, the following modifications were implemented in order to  
99 achieve increased stability for long term climate simulations (Elguindi et al. 2017  
100 document any modifications which follow the choice of the non-hydrostatic dynamical  
101 core through the namelist parameter *idynamic* = 2; further available user-dependant  
102 options, and the corresponding section in the namelist, are explicitly indicated):

103

104 i) The reference state temperature profile is computed using a latitude dependent  
105 climatological temperature distribution and thus is a function of the specific domain  
106 coordinates (*base\_state\_pressure*, *logp\_lrate* parameters in *&referenceatm*) (Elguindi et  
107 al. 2017). These two parameters were hard-coded in the original MM5 while for the  
108 RegCM are user configurable;

109

110 ii) The lateral time dependent boundary conditions (*iboudy* in *&physicsparam*) for each  
111 prognostic variable use the same exponential relaxation technique (*iboudy* = 5) described  
112 in Giorgi et al. (1993). The linear MM5 relaxation scheme is also kept as an option (*iboudy*  
113 = 1);

114

115 iii) The advection term in the model equations, which in the MM5 code is implemented  
116 using a centered finite difference approach, was changed to include a greater upstream  
117 weight factor as a function of the local Courant number (Elguindi et al. 2017). The  
118 maximum value of the weight factor is user configurable (*uoffc* in *&dynparam*). As detailed

119 in the MM5 model description (Grell et al, 1995), the horizontal advection term for a scalar  
120 variable  $X$  contributes to the total tendency as:

121

$$122 \Delta_{adv} (p^* X)_G = -m^2|_G \left[ \frac{(p^* X|_b \frac{u}{m}|_b - p^* X|_a \frac{u}{m}|_a)}{dx} + \frac{(p^* X|_d \frac{v}{m}|_d - p^* X|_c \frac{v}{m}|_c)}{dy} \right]$$

123

124 where the  $m$  is the projection mapping factor and, with respect to Figure 1, assuming that  
125 the computation is to be performed for the gold cross point  $G$ , the averages are performed  
126 in the points  $a, b, c, d$ . For the  $u/m$  and  $v/m$  terms, the average value is computed using  
127 respectively the values in points  $AC, BD, CD, AB$ .

128 In RegCM4 for the term  $p^* X$ , the model computes a weighted average value of the field  
129 using the value in gold+cyan and gold+green cross points with weights increasing the  
130 relative contribution of the upstream point up as a function of the local courant number:

131

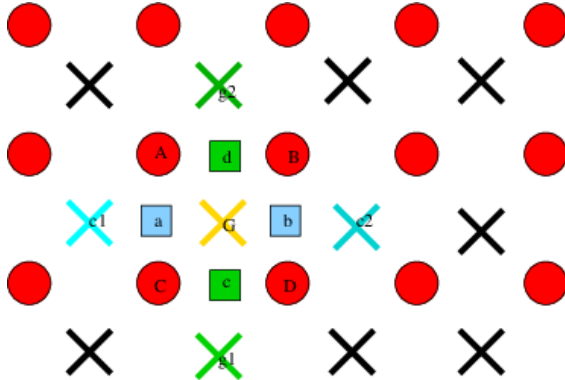
$$132 p^* X|_a = 0.5((1 - f_1)p^* X|_G + (1 + f_1)p^* X|_{c_1})$$
$$133 p^* X|_b = 0.5((1 - f_1)p^* X|_{c_2} + (1 + f_1)p^* X|_G)$$
$$134 p^* X|_c = 0.5((1 - f_2)p^* X|_G + (1 + f_2)p^* X|_{g_1})$$
$$135 p^* X|_d = 0.5((1 - f_2)p^* X|_{g_2} + (1 + f_2)p^* X|_G)$$

136 where  $f_1, f_2$  are defined as the local Courant number for the 1D advection equations  
137 multiplied for a control factor:

138

$$139 f_1 = \mu_{fc} dt \frac{(u|_a + u|_b)}{2dx}$$
$$140 f_2 = \mu_{fc} dt \frac{(v|_c + v|_d)}{2dy};$$

141



142

143 **Figure 1 Schematic representation showing the horizontal advection scheme**  
 144 **staggering. Circles are U,V points. X are scalar variable points.**

145

146 iv) The water species (cloud, ice, rain, snow) term uses the same advection scheme as  
 147 the other variables (Elguindi et al. 2017) and not a complete upstream scheme as in the  
 148 MM5 code (Grell et al. 1995);

149

150 v) A local flux limiter reduces the advection terms in order to remove unrealistic strong  
 151 gradients and its limits are user configurable (in the *&dynparam* section the maximum  
 152 gradient fraction for advection: temperature, *t\_extrema*, specific humidity, *q\_rel\_extrema*,  
 153 liquid cloud content, *c\_rel\_extrema* and for tracers, *t\_rel\_extrema*). This was hardcoded  
 154 in the MM5 code and the limits were not user configurable;

155

156 vi) The diffusion stencil of the Laplace equation uses a nine point approach as in LeVeque  
 157 (2006) and a topography dependent environmental diffusion coefficient is added to  
 158 reduce spurious diffusion along pressure coordinate slopes (Elguindi et al. 2017) as in  
 159 the hydrostatic version of the code (Giorgi et al. 1993b). The change in stencil does not  
 160 affect the overall fourth order precision of the model, but reduces the computational  
 161 stencil size, thus reducing the communication overhead;

162

163 vii) The top boundary radiative condition (*ifupr = 1* in *&nonhydroparam*) adopted in the  
 164 semi-implicit vertical differencing scheme to reduce the reflection of energy waves uses  
 165 coefficients on a 13x13 matrix which are re-computed every simulation day and not kept  
 166 constant throughout the whole simulation as in the MM5 code. This allows the model to

167 be run for longer simulation times while not being strongly tied to the intial atmospheric  
168 conditions;

169

170 viii) The dynamical control parameter  $\beta$  in the semi-implicit vertical differencing scheme  
171 (*nhbet* in *&nonhydroparam*) used for acoustic wave damping (Elguindi et al. 2017) is user  
172 configurable (Klemp and Dudhia, 2008), while it is hard-coded in the MM5;

173

174 ix) A Rayleigh damping (*ifrayd* = 1 in *&nonhydroparam*) of the status variables towards  
175 the input GCM boundary conditions can be activated in the top layers (*rayndamp*  
176 configuring the number of top levels to apply) with a configurable relaxation time  
177 (*rayalpha0*, Klemp and Lilly, 1978, Durran and Klemp, 1983. This is consistent to what is  
178 implemented in the WRF model);

179

180 x) The water species time filtering uses the Williams (2009) modified filter with  $\alpha = 0.53$   
181 instead of the RA filter used by all the other variables. The  $v$  factor in the RA filter is user  
182 configurable (*gnu1* and *gnu2* in *&dynparam*). This reduces the damping introduced by the  
183 Robert-Asselin filter and the computational diffusion introduced by the horizontal  
184 advection scheme.

185

186 With these modifications, the model basic equations, under leap-frog integration scheme,  
187 are (Elguindi et al. 2017) :

188

189

$$\frac{\partial p^* u}{\partial t} = -m^2 \left[ \frac{\partial p^* uu/m}{\partial x} + \frac{\partial p^* vu/m}{\partial y} \right] - \frac{\partial p^* u \dot{\sigma}}{\partial \sigma} + u DIV - \frac{mp^*}{\rho} \left[ \frac{\partial p'}{\partial x} - \frac{\sigma}{p^*} \frac{\partial p^*}{\partial x} \frac{\partial p'}{\partial \sigma} \right] + p^* fv - p^* ew \cos \theta + D_u \quad (1)$$

190

191

$$\frac{\partial p^* v}{\partial t} = -m^2 \left[ \frac{\partial p^* uv/m}{\partial x} + \frac{\partial p^* vv/m}{\partial y} \right] - \frac{\partial p^* v \dot{\sigma}}{\partial \sigma} + v DIV - \frac{mp^*}{\rho} \left[ \frac{\partial p'}{\partial y} - \frac{\sigma}{p^*} \frac{\partial p^*}{\partial y} \frac{\partial p'}{\partial \sigma} \right] - p^* fu + p^* ew \sin \theta + D_v \quad (2)$$

192

193

$$\frac{\partial p^* w}{\partial t} = -m^2 \left[ \frac{\partial p^* uw/m}{\partial x} + \frac{\partial p^* vw/m}{\partial y} \right] - \frac{\partial p^* w \dot{\sigma}}{\partial \sigma} + w DIV + \\ p^* g \frac{\rho_0}{\rho} \left[ \frac{1}{p^*} \frac{\partial p'}{\partial \sigma} + \frac{T'_v}{T} - \frac{T_0 p'}{T p_0} \right] - p^* g [(q_c + q_r)] + p^* e (u \cos \theta - v \sin \theta) + D_w \quad (3)$$

194

195

$$\frac{\partial p^* p'}{\partial t} = -m^2 \left[ \frac{\partial p^* up'/m}{\partial x} + \frac{\partial p^* vp'/m}{\partial y} \right] - \frac{\partial p^* p' \dot{\sigma}}{\partial \sigma} + p' DIV - \\ m^2 p^* \gamma p \left[ \frac{\partial u/m}{\partial x} - \frac{\sigma}{mp^*} \frac{\partial p^*}{\partial x} \frac{\partial u}{\partial \sigma} + \frac{\partial v/m}{\partial y} - \frac{\sigma}{mp^*} \frac{\partial p^*}{\partial y} \frac{\partial v}{\partial \sigma} \right] + \rho_0 g \gamma p \frac{\partial w}{\partial \sigma} + p^* \rho_0 g \quad (4)$$

196

197

$$\frac{\partial p^* T}{\partial t} = -m^2 \left[ \frac{\partial p^* uT/m}{\partial x} + \frac{\partial p^* vT/m}{\partial y} \right] - \frac{\partial p^* T \dot{\sigma}}{\partial \sigma} + T DIV + \\ \frac{1}{\rho c_p} \left[ p^* \frac{Dp'}{Dt} - \rho_0 g p^* w - D_{p'} \right] + p^* \frac{\dot{Q}}{c_p} + D_T \quad (5)$$

199

200 Where:

$$DIV = m^2 \left[ \frac{\partial p^* u/m}{\partial x} + \frac{\partial p^* v/m}{\partial y} \right] + \frac{\partial p^* \dot{\sigma}}{\partial \sigma}$$

201

$$\dot{\sigma} = -\frac{\rho_0 g}{p^*} w - \frac{m\sigma}{p^*} \frac{\partial p^*}{\partial x} u - \frac{m\sigma}{p^*} \frac{\partial p^*}{\partial y} v$$

202

$$\tan \theta = -\cos \phi \frac{\partial \lambda / \partial y}{\partial \phi / \partial x}$$

203

$$p(x, y, z, t) = p_0(z) + p'(x, y, z, t)$$

$$T(x, y, z, t) = T_0(z) + T'(x, y, z, t)$$

204

$$\rho(x, y, z, t) = \rho_0(z) + \rho'(x, y, z, t)$$

205

206 with the vertical sigma coordinate defined as:

207

$$\sigma = \frac{(p_0 - p_t)}{(p_s - p_t)}$$

208

209

210 where  $p_s$  is the surface pressure and  $p_0$  is the reference pressure profile. The total  
211 pressure

212 at each grid point is thus given as:

213

214 
$$p(x, y, z, t) = p^* \sigma(k) + p_t + p'(x, y, z, t)$$

215

216 With  $p_t$  being the top model pressure assuming a fixed rigid lid.

217 The model physics schemes for boundary layer, radiative transfer, land and ocean  
218 surface processes, cloud and precipitation processes are extensively described in Giorgi  
219 et al. (2012) and summarized in Table 1. For each physics component a number of  
220 parameterization options are available (Table 1), and can be selected using a switch  
221 selected by the user. As mentioned, the use of non-hydrostatic dynamics is especially  
222 important when going to convection-permitting resolutions of a few km (Prein et al. 2015).  
223 At these resolutions the scale separation assumption underlying the use of cumulus  
224 convection schemes is not valid any more, and explicit cloud microphysics  
225 representations are necessary. The RegCM4 currently includes two newly implemented  
226 microphysics schemes, the Nogherotto-Tompkins (Nogherotto et al. 2016) and the WSM5  
227 scheme from the Weather Research Forecast (WRF, Skamarok et al. 2008) model, which  
228 are briefly described in the next sections for information to model users.

229

Model physics (Namelist flag)	Options	n. option	Reference
<b>Dynamical core</b> ( <b>idynamic</b> )	Hydrostatic	1	Giorgi et al. 1993a,b Giorgi et al. 2012
	Non-Hydrostatic (*)	2	present paper
<b>Radiation</b> ( <b>irrtm</b> )	CCSM	0	Kiehl et al. 1996
	RRTM (*)	1	Mlawer et al. 1997

<b>Microphysics</b> <b>(ipptls)</b>	Subex	1	Pal et al 2000
	Nogherotto Thompkins	2	Nogherotto et al. 2016
	WSM5 (*)	3	Hong et al 2004
<b>Cumulus</b> <b>(icup)</b>	Kuo	1	Anthes et al. 1987
	Grell	2	Grell 1993
	Emanuel	4	Emanuel 1991
	Tiedtke	5	Tiedtke 1989, 1993
	Kain-Fritsch	6	Kain and Fritsch, 1990; Kain 2004
	MM5 Shallow cumulus (only mixing) (*)	-1	Grell et al. 1994
<b>Planetary Boundary Layer</b> <b>(ibltyp)</b>	Modified-Holtslag	1	Holtslag et al., 1990
	UW	2	Bretherton et al. 2004
<b>Land Surface</b> <b>(code compiling option)</b>	BATS	/	Dickinson et al. 1993; Giorgi et al. 2003
	CLM4.5	/	Oleson et al. 2013
<b>Ocean Fluxes</b> <b>(iocnflux)</b>	BATS	1	Dickinson et al. 1993
	Zeng	2	Zeng et al. 1998
	COARE	3	Fairall et al. 1996a,b

<b>Interactive lake (lakemod)</b>	1D diffusion/convection	1	Hostetler et al. 1993
<b>Tropical band (i_band)</b>	RegT-Band	1	Coppola et al. 2012
<b>Coupled ocean (iocncpl)</b>	RegCM-ES	1	Sitz et al. 2017

230 **Table 1 Core and sub-grid physics scheme available in RegCM-NH. New schemes  
231 available with this release are starred (\*).**

232

233

234 **Explicit microphysics schemes:**

235

236 *Nogherotto-Tompkins Scheme:*

237 A new parameterization for explicit cloud microphysics and precipitation built upon the  
238 European Centre for Medium Weather Forecast's Integrated Forecast System (IFS)  
239 module (Tiedtke, 1993, Tompkins, 2007), was introduced in RegCM4 (*ipptls* = 2 in  
240 *&microparam*) by Nogherotto et al. (2016). In the present configuration, the scheme  
241 implicitly solves 5 prognostic equations for water vapor, qr, cloud liquid water, ql, rain, qr,  
242 cloud ice, qi, and snow, qs, but it is also easily extendable to a larger number of variables.  
243 Water vapor, cloud liquid water, rain, cloud ice and snow are all expressed in terms of the  
244 grid-mean mixing ratio.

245 Cloud liquid and ice water content are independent, allowing the existence of supercooled  
246 liquid water and mixed-phase clouds. Rain and snow precipitate with a fixed terminal fall  
247 speed and can then be advected by the three dimensional winds. A check for the  
248 conservation of enthalpy and of total moisture is ensured at the end of each timestep. The  
249 governing equation for each variable is:

250

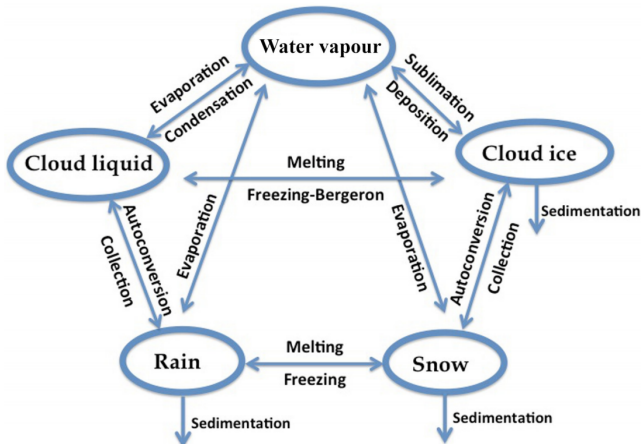
$$\frac{\partial q_x}{\partial t} = S_x + \frac{1}{\rho} \frac{\partial}{\partial z} (\rho V_x q_x)$$

251

252

253 The local variation of the mixing ratio  $q_x$  of the variable  $x$  is given by the sum of  $S_x$ ,  
 254 containing the net sources and sinks of  $q_x$  through microphysical processes (i.e.  
 255 condensation, evaporation, auto-conversion, melting, etc.), and the sedimentation term,  
 256 which is a function of the fall speed  $V_x$ . An upstream approach is employed to solve the  
 257 equations. The sources and sinks contributors are divided in two groups according to the  
 258 duration of the process they describe: processes that are considered to be fast relative to  
 259 the model time step are treated implicitly while slow processes are treated explicitly. The  
 260 processes taken into account (shown in Figure 2) are the microphysical pathways across  
 261 the 5 water variables: condensation, autoconversion, evaporation, cloud water collection  
 262 (accretion), and autoconversion for warm clouds, and freezing, melting, deposition,  
 263 sublimation for cold clouds.

264



265

266 **Figure 2: Depiction of the new scheme, showing the five prognostic variables and**  
 267 **how they are related to each other through microphysical processes**

268 For each microphysical pathway, phase changes are associated with the release or  
 269 absorption of latent heat, which then impacts the temperature budget. The impact is

270 calculated using the conservation of liquid water temperature  $T_L$  defined as:

271

272

$$T_L = T - \frac{L_v}{C_p}(q_l + q_r) - \frac{L_s}{C_p}(q_i + q_s).$$

273 Given that  $dT_L = 0$ , the rate of change of the temperature is given by the following  
274 equation:

275

276

$$\frac{\partial T}{\partial t} = \sum_{x=1}^m \frac{L(x)}{C_p} \left( \frac{dq_x}{dt} - D_{q_x} - \frac{1}{\rho} \frac{\partial}{\partial z} (\rho V_x q_x) \right)$$

277

278 where  $L(x)$  is the latent heat of fusion or evaporation, depending on the process  
279 considered,  $Dq_x$  is the convective detrainment and the third term in brackets is the  
280 sedimentation term.

281 At the end of each time step a check is carried out of the conservation of total water and  
282 moist static energy:

283

$$h = C_P T + gz + L q_x.$$

284 The scheme is tunable through parameters in the *&microparam* section of the namelist  
285 (RegCM-4.7.1/Doc/README.namelist; Elguindi et al. 2017).

286 WSM5 Scheme:

287 RegCM4-NH also employs the Single-Moment 5-class microphysics scheme of the WRF  
288 model (Skamarock et al., 2008). This scheme (*ipptls* = 3 in *&microparam*) follows Hong  
289 et al. (2004) and, similarly to Nogherotto et al. (2016), includes vapor, rain, snow, cloud  
290 ice, and cloud water hydrometeors. The scheme separately treats ice and water  
291 saturation processes, assuming water hydrometeors for temperatures above freezing,  
292 and cloud ice and snow below the freezing level (Dudhia, 1989, Hong et al., 1998). It  
293 accounts for supercooled water and a gradual melting of snow below the melting layer  
294 (Hong et al., 2004, and Hong and Lim, 2006). Therefore, the WSM5 and Nogherotto-  
295 Tompkins schemes have similar structures (Figure 2), but also important differences.

296 Differently from the Nogherotto-Tompkins scheme, the WSM5 (as well as the other WSM  
297 schemes in WRF) prescribes an inverse exponential continuous distribution of particle  
298 size (ex. Marshall and Palmer (1948) for rain, Gunn and Marshall (1958) for snow). It also  
299 includes the size distribution of ice particles and, as a major novelty, the definition of the  
300 number of ice crystals based on ice mass content rather than temperature. Both the  
301 Nogherotto-Tompkins and WSM5 schemes include autoconversion, i.e. sub-time step  
302 processes of conversion of cloud water to rain and cloud ice to snow. For rain, Hong et  
303 al. (2004) use a Kessler (1969) type algorithm in WSM5, but with a stronger physical basis  
304 following Tripoli and Cotton (1980). The Nogherotto-Tompkins scheme also includes the  
305 original Kessler (1969) formula as an option, but it makes available other three  
306 exponential approaches following Sundqvist et al. (1989), Beheng (1994), and  
307 Khairoutdinov and Kogan (2000). For ice autoconversion the Nogherotto-Tompkins  
308 scheme uses an exponential approach (Sundqvist, 1989) with a specific coefficient for ice  
309 particles (following Lin et al., 1983) depending on temperature, while the WSM5 uses a  
310 critical value of ice mixing ratio (depending on air density) and a maximum allowed ice  
311 crystal mass (following Rutledge and Hobbs, 1983) that suppresses the process at low  
312 temperatures because of the effect of air density. Finally, the WSM5 has no dependency  
313 on cloud cover for condensation processes while the Nogherotto-Tompkins scheme uses  
314 cloud cover to regulate the condensation rate in the formation of stratiform clouds.

315

316 **Illustrative case studies**

317

318 Three case studies (Table 2) of Heavy Precipitation Events (HPE) have been identified in  
319 order to test and illustrate the behavior of the non-hydrostatic core of the RegCM4-NH,  
320 with focus on the explicit simulation of convection over different regions of the world. In  
321 two test cases, California and Lake Victoria, data from the ERA-Interim reanalysis (Dee  
322 et al. 2011) are used to provide initial and lateral meteorological boundary conditions for  
323 an intermediate resolution run (grid spacing of 12 km, with use of convection  
324 parameterizations) (Figure 3), which then provides driving boundary conditions for the  
325 convection-permitting experiments. In the Texas case study, however, we nested the  
326 model directly in the ERA-Interim reanalysis with boundary conditions provided every 6  
327 hours, given that such configuration was able to reproduce accurately the HPE intensity.  
328 In this case the model uses a large LBC relaxation zone which allows the description of  
329 realistic fine-scale features driving this weather event (even if not fully consistent with the  
330 Matte et al. (2017) criteria). All simulations start 24-48 hours before the HPE. The analysis  
331 focuses on the total accumulated precipitation over the entire model domain at 3 km  
332 resolution (Fig. 3) for the periods defined in Table 2. In the cases of California and Texas  
333 the evaluation also includes the time series of 6 hourly accumulated precipitation  
334 averaged on the region of maximum precipitation (black rectangles in Figs. 3) against  
335 available high temporal resolution observations (NCEP/CPC) (Table 3). The discussion  
336 of the case studies is presented in the next sections; the configuration files (namelists)  
337 with full settings for the three test cases are available at  
338 <https://zenodo.org/record/5106399>.

339

340 A key issue concerning the use of CP-RCMs is the availability of very high resolution,  
341 high quality observed datasets for the assessment and evaluation of the models, which  
342 is not there for most of the world regions. Precipitation measurements come from  
343 essentially three distinct sources: in-situ rain-gauges, ground radar and satellite. In the  
344 present study we use 7 observational datasets depending on the case study and the area

345 covered, as described in Table 2. We have used: Precipitation Estimation from Remotely  
 346 Sensed Information using Artificial Neural Networks - Climate Data Record (PERSIAN-  
 347 CDR), Climate Hazards Group InfraRed Precipitation with Station data (CHIRPS), the  
 348 Climate Prediction Center morphing method (CMORPH), Tropical Rainfall Measuring  
 349 Mission (TRMM), NCEP/CPC-Four Kilometer Precipitation Set Gauge and Radar  
 350 (NCEP/CPC), CPC-Unified daily gauge based precipitation estimates (CPC) and  
 351 Parameter-elevation Regressions on Independent Slopes Model (PRISM) (Table 3).  
 352 NCEP/CPC is a precipitation analysis which merges a rain gauge dataset with radar  
 353 estimates. CMORPH and PERSIAN-CDR are based on satellite measurements, CHIRPS  
 354 incorporates satellite imagery with in-situ station data. CPC is a gauge-based analysis of  
 355 daily precipitation and the PRISM dataset gathers climate observations from a wide range  
 356 of monitoring networks, applies sophisticated quality control measures, and develops  
 357 spatial climate datasets incorporating a variety of modeling techniques at multiple spatial  
 358 and temporal resolutions.

359

Case	ACRONYM	Region of The event	Domains size lon x lat x vertical levels	Simulation Time Window
1	CAL	California	480 x 440 x 41	15 Feb 2004 00:00 19 Feb 2004 00:00
2	TEX	Texas	480 x 440 x 41	9 June 2010 00:00 12 June 2010 00:00
3	LKV	Lake Victoria	550 x 530 x 41	25 Nov 1999 00:00

				1 Dec 1999 00:00
--	--	--	--	---------------------

360 **Table 2: List of acronyms and description of the test cases with corresponding 3km  
361 domain sizes and simulation period.**

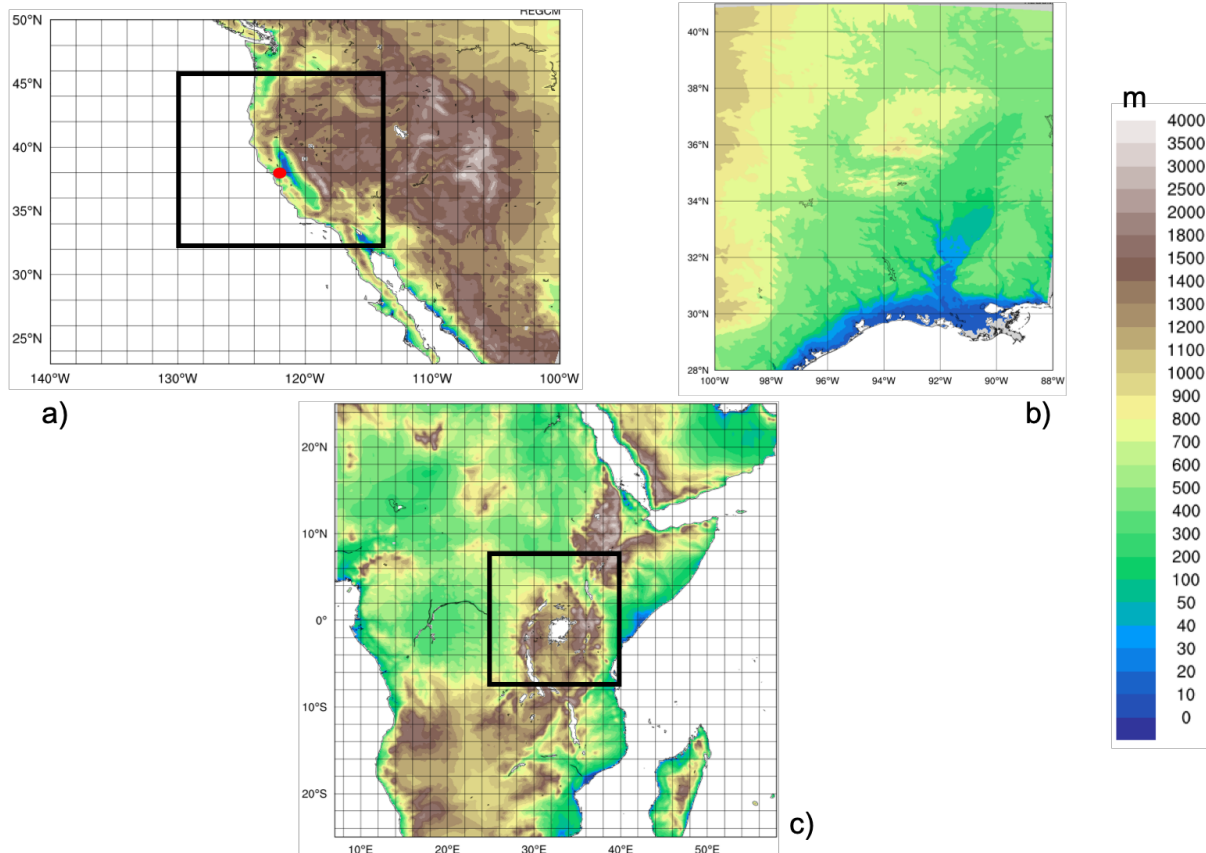
362

Dataset name	Region	Spatial Resolution	Temporal Resolution	Data Source	Reference
TRMM	World	0.5°	Daily	Satellite	Huffman et al. (2007)
CHIRPS	World	0.05°	Daily	Station data+Satellite	Funk et al. (2015)
CMORPH	World	0.25°	Daily	Satellite	Joyce et al. (2004)
NCEP/CPC	USA	0.04°	Hourly	Gauge and Radar	<a href="https://doi.org/10.5065/D69Z93M3">https://doi.org/10.5065/D69Z93M3</a> . Accessed: 27/06/2018
CPC	World	0.5°	Daily	Station data	Chen and Xie (2008)
PRISM	USA	0.04°	Daily	Station data	PRISM Climate Group. 2016.

PERSIAN- CDR	World	0.25°	Daily	Satellite	Ashouri et al. (2015)
-----------------	-------	-------	-------	-----------	--------------------------

363 **Table 3: List of observed precipitation datasets used for comparison.**

364



365

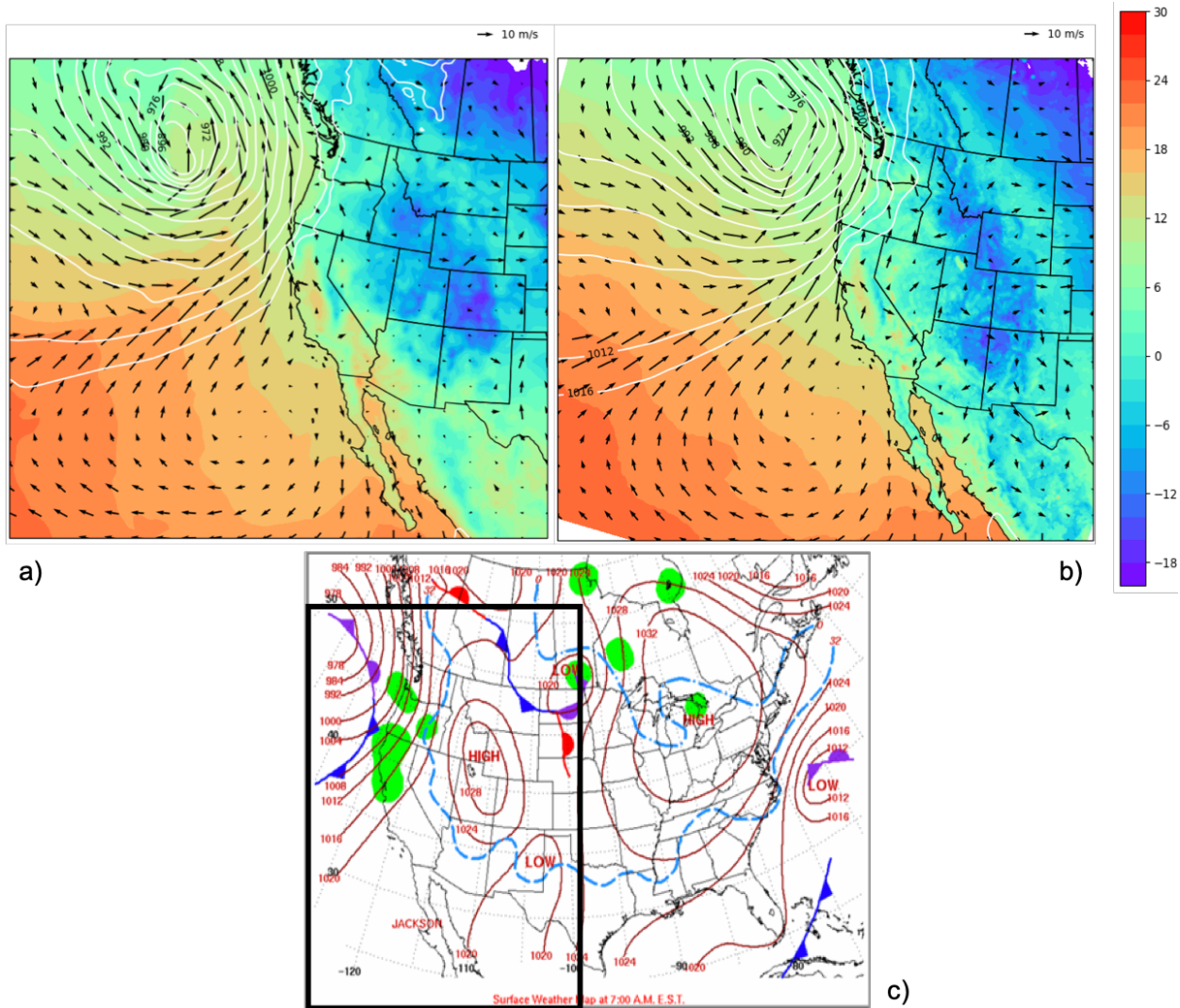
366 **Figure 3: Simulation domains tested, a) California (CAL), b) Texas (TEX), c) Lake**  
 367 **Victoria (LKV). For CAL (a) and LKV (b) the black square shows the 3 km simulation**  
 368 **domains nested in the 12 km domain in figure. For TEX the 3 km domain simulation**  
 369 **(c) is fed directly with the ERA-Interim reanalysis fields.**

370

371

372 **California**

373 The first case, referred to as CAL (California) in Table 2, is a HPE which occurred on 16–  
374 18 February 2004, producing flooding conditions for the Russian River, a southward-  
375 flowing river in the Sonoma and Mendocino counties of northern California (red-dot)  
376 (Figure 3). The event is documented in detail by Ralph et al. (2006), who focused their  
377 attention on the impact of narrow filament-shaped structures of strong horizontal water  
378 vapor transport over the eastern Pacific Ocean and the western U.S. coast, called  
379 Atmospheric Rivers (ARs). ARs are typically associated with a low-level jet stream ahead  
380 of the cold front of extratropical cyclones (Zhu and Newell 1998; Dacre et al. 2015; Ralph  
381 et al. 2018), and can induce heavy precipitation where they make landfall and are forced  
382 to rise over mountain chains (Gimeno et al. 2014). The CAL event consists of a slow  
383 propagating surface front arching southeastward towards Oregon and then  
384 southwestward offshore of California (Fig.3a,c). Rain began over the coastal mountains  
385 of the Russian River watershed at 0700 UTC, 16 February, as a warm front descended  
386 southward, and also coincided with the development of orographically favoured low-level  
387 upslope flow Ralph et al. (2006).



388

389 **Figure 4: Mean sea level pressure (mslp) (white contour lines), surface temperature  
390 (color shading) and 100-m wind direction (black arrows) at 7:00 UTC, 16 Feb. 2004  
391 of ERA5 reanalysis (a) and RegCM 12km (b) respectively. (c) NCEP-NOA Surface  
392 Analysis of pressure and fronts . The black box in (c) bounded the area represented  
393 in (a) and (b)**

394 The intermediate resolution (12 km) domain (Figure 3a) covers a wide area  
 395 encompassing California and a large portion of the coastal Pacific Ocean, with 23 vertical  
 396 levels and a parameterization for deep convection based on the Kain–Fritsch scheme  
 397 (Kain, 2004). The ERA-Interim driven simulation is initialized at 0000 UTC, 15 February  
 398 2004 (Table 2) and lasts until 0000 UTC 19 February 2004. This simulation drives a

399 corresponding RegCM4-NH run using a smaller domain centered over northern California  
400 (Fig. 3a) at 3 km horizontal grid spacing and 41 vertical levels, with boundary conditions  
401 updated at 6 hour intervals. In RegCM4-NH only the shallow convection component of  
402 the Tiedtke scheme (Tiedtke, 1996) is activated. Simulated precipitation is compared with  
403 the CHIRPS, CMORPH, TRMM, PRISM, NCEP/CPC observations described in Table 3.

404 First, we notice that the synoptic conditions characteristic of this case study, which are  
405 fed into the RegCM4-NH model, are well reproduced by RegCM4 at 12 km, as shown in  
406 Figure 4, where we compare the mean sea level pressure (mslp), surface temperature  
407 and wind direction on 14 Feb at 7:00 am, as simulated by RegCM at 12 km (Fig.3b) with  
408 corresponding fields from the ERA5 reanalysis (Fig.4a).The surface analysis of pressure  
409 and fronts derived from the operational weather maps prepared at the National Centers  
410 for Environmental Prediction, Hydrometeorological Prediction Center, National Weather  
411 Service ([https://www.wpc.ncep.noaa.gov/dailywxmap/index\\_20040216.html](https://www.wpc.ncep.noaa.gov/dailywxmap/index_20040216.html)) is also  
412 reported in Figure 4c.

413 The observed precipitation datasets show similar patterns for the total accumulated  
414 precipitation (Figure 5), in particular CHIRPS, PRISM and NCEP exhibit similar spatial  
415 details and magnitudes of extremes. CHIRPS places a maximum around 42°N which is  
416 not found in the other datasets. CMORPH and TRMM show lower precipitation maxima  
417 and lesser spatial details due to their lower resolution, indicating that the performance of  
418 satellite-based products may be insufficient as a stand alone product to validate the model  
419 for this case.

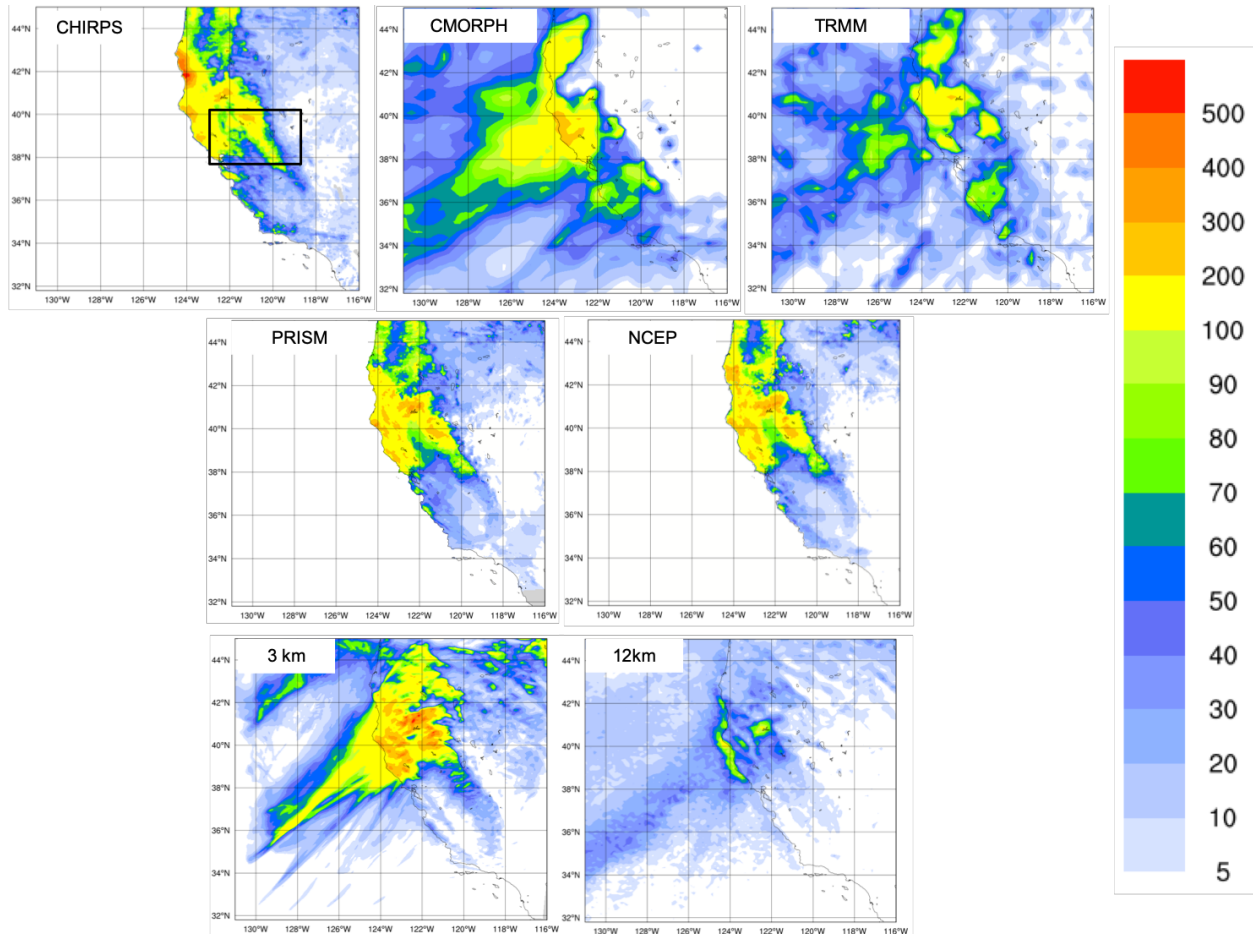
420

421 In general, the observed precipitation datasets place the highest maxima on the terrain  
422 peaks, with extreme rainfall greater than 250 mm in 60 hours over the coastal mountains  
423 and greater than 100 – 175 mm elsewhere (Fig. 5a). The black box in Fig 5 shows the  
424 area of the Russian River watershed, highlighting the locations of the observing systems,  
425 including Cazadero (CZD) and Bodega Bay (BBY) where the largest rainfall rates were  
426 detected, 269 mm and 124 mm in 60-h accumulated rainfall between 0000 UTC 16  
427 February and 1200 UTC 18 February 2004, respectively (Ralph et al., 2006).

428 The convection-permitting simulation captures the basic features of the observed  
429 precipitation , as shown for example in Fig.5, both in terms of spatial distribution and  
430 temporal evolution of rainfall (Fig.6a). However, it shows higher precipitation rates than  
431 observed over the sea and over the mountain chains, with lower intensities than observed  
432 in the south-east part of the mountain chain (Fig.5). By contrast, the 12-km simulation  
433 severely underestimates the magnitude of the precipitation event (Fig.5).

434 Concerning the timing and intensity of the event in the CZD subregion, 6-hourly  
435 accumulated precipitation (Fig.6a) averaged over the black box of Figure 5, shows that  
436 both the 3 km and 12 km simulations capture the onset of the event, but the peak intensity  
437 is strongly underestimated by the 12 km run, while it is well simulated by the 3 km run,  
438 although the secondary maximum is overestimated. Therefore, our results demonstrate  
439 that only the high resolution convection-permitting model captures this extreme event,  
440 and that parameterized convection has severe limits in this regard (Done et al. 2004; Lean  
441 et al. 2008; Weisman et al. 2008; Weusthoff et al. 2010; Schwartz 2014; Clark et al. 2016).

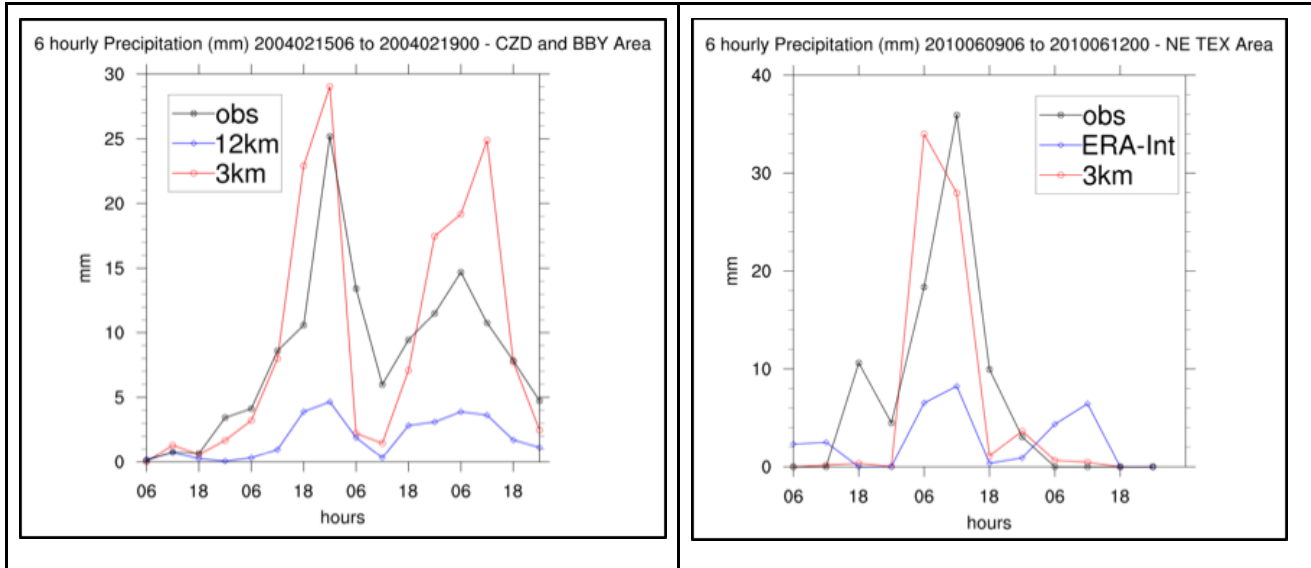
442



443

444 **Figure 5 : Total accumulated precipitation (mm) during the California case:**  
 445 **CHIRPS, CMORPH, TRMM observations (top line), PRISM and NCEP Reanalysis**  
 446 **(middle line) and convection-permitting simulation with RegCM4-NH at 3km and**  
 447 **RegCM4 at 12km (bottom line) .The black box denotes the area where the spatial**  
 448 **average of 6-hourly accumulated precipitation is calculated and reported in Fig. 6.**

CAL (a)	TEX (b)
---------	---------



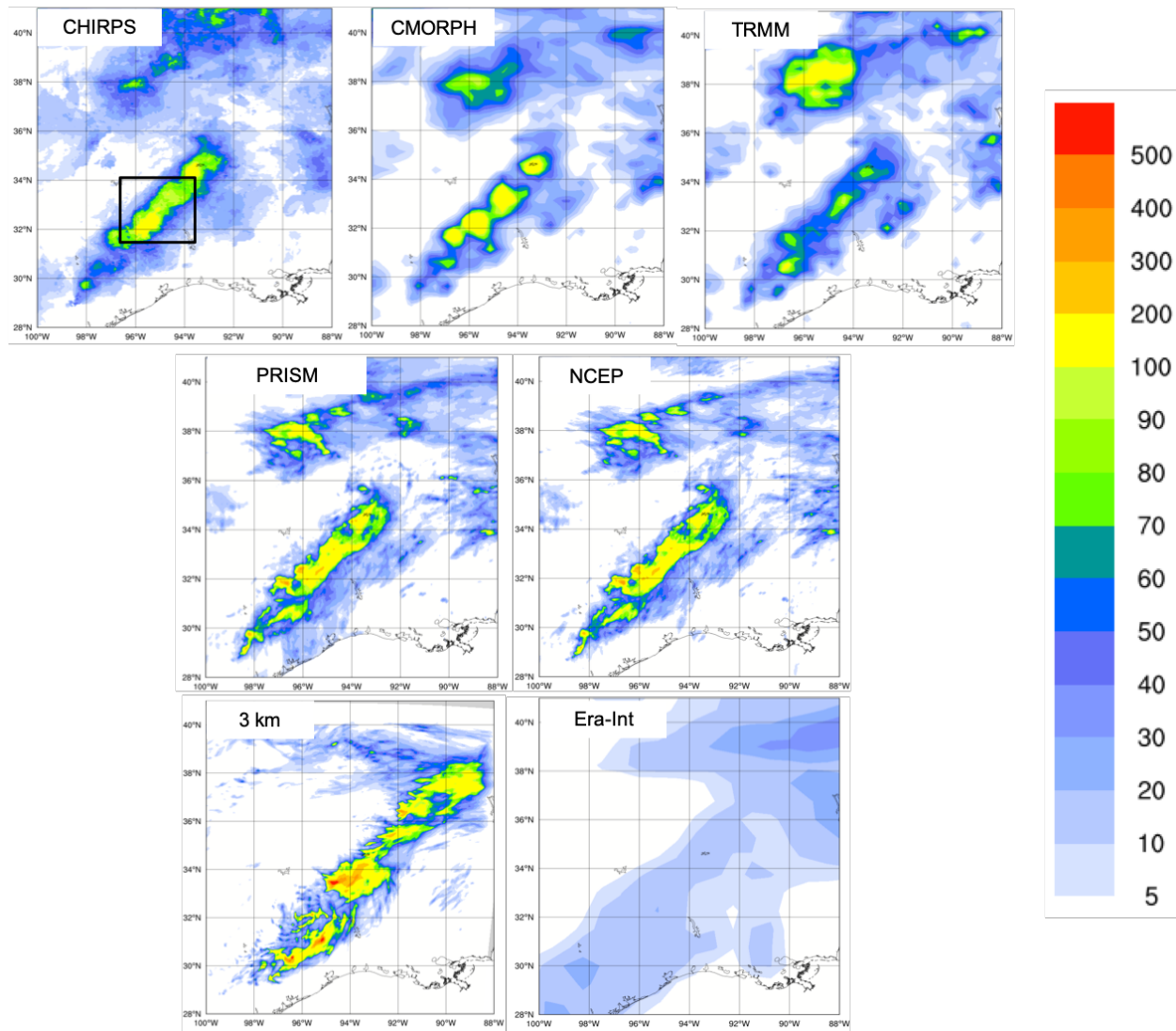
449 **Figure 6: Time series of the 6 hourly accumulated precipitation (in mm on the y-**  
 450 **axis) during the CAL event (a) and during the TEX event (b). The blue lines show**  
 451 **RegCM4 12 Km and ERA interim 6 hourly accumulated precipitation averaged over**  
 452 **the areas indicated by the red square in Figure 3 (a,b) while the red line shows the**  
 453 **6 hourly accumulated precipitation simulated by RegCM4-NH. The observations are**  
 454 **shown with a black line.**

455

456 **Texas**

457 Case 2, hereafter referred to as TEX (Table 2), is a convective precipitation episode  
 458 exhibiting characteristics of the “Maya Express” flood events, linking tropical moisture  
 459 plumes from the Caribbean and Gulf of Mexico to midlatitude flooding over the central  
 460 United States (Higgins 2011). During the TEX event, an upper-level cutoff low over  
 461 northeastern Texas, embedded within a synoptic-scale ridge, moved slowly  
 462 northeastward. Strong low-level flow and moisture transport from the western Gulf of  
 463 Mexico progressed northward across eastern Texas. The event was characterized by  
 464 low-level moisture convergence, weak upper-level flow, weak vertical wind shear, and  
 465 relatively cold air (center of cutoff low), which favored the slow-moving convective storms  
 466 and nearly stationary thunderstorm outflow boundaries. The main flooding event in

467 eastern Texas occurred on June 10, 2010, with a daily maximum rainfall of 216.4 mm of  
468 the region in the black box of Figure 7 (Higgins 2011).



469  
470 **Figure 7: Total accumulated precipitation (mm) during the Texas case: CHIRPS,**  
471 **CMORPH, TRMM observations (top line), PRISM and NCEP Reanalysis (central line)**  
472 **and convection-permitting simulation with RegCM4-NH at 3 km grid spacing and**  
473 **Era-Int (bottom line). The black box shows the area where the spatial average of 6-**  
474 **hourly accumulated precipitation was calculated and reported in Figure 6.**

475  
476 As for the California case, the observed precipitation datasets show coherent patterns for  
477 the total accumulated precipitation (Fig. 6), with the highest values related to the

478 mesoscale convective system in eastern Texas (~ 200 mm), and another smaller area of  
479 high precipitation more to the north, approximately over Oklahoma. PRISM and NCEP  
480 capture similar spatial details and magnitudes of extremes, CHIRPS has lower  
481 precipitation extremes in the north compared to the other datasets, while CMORPH and  
482 TRMM show the lowest precipitation extremes and reduced spatial details as already  
483 noted for the California case.

484 The bottom panels in Figure 7 present precipitation as produced by the RegCM4-NH and  
485 the ERA-Interim reanalysis (driving data) , respectively. ERA-Interim reproduces some of  
486 the observed features of precipitation, but with a substantial underestimation over the  
487 areas of maximum precipitation because of its coarse resolution. By comparison, the  
488 RegCM4-NH simulation (Fig. 7) shows an improvement in both pattern and intensity of  
489 precipitation, and is substantially closer to observations over eastern Texas. However,  
490 the precipitation area is slightly overestimated and the model is not capable of  
491 reproducing the small region of maximum precipitation in the north.

492

493 The time series of precipitation over eastern Texas from 9 to 12 June 2010 for  
494 observations (black line), ERA-Interim (blue line) and RegCM4-NH (red line) are reported  
495 in Figure 6b. Precipitation increases over this region from 00:00, 10 June, until it reaches  
496 the observed maximum at 12:00, 10 June (~35 mm), gradually decreasing afterwards  
497 until 6:00, 11 June. The RegCM4-NH simulation shows a more realistic temporal  
498 evolution than the ERA-Interim, which exhibits an overall underestimation of precipitation.  
499 In general, the non-hydrostatic model produces precipitation values close to the  
500 observations, however, the simulated maximum is reached 6 hours earlier than observed.

501

502

### 503 **Lake Victoria**

504 Case 3 focuses on Lake Victoria (LKV), with the purpose of testing RegCM4-NH on a  
505 complex and challenging region in terms of convective rainfall. It is estimated that each  
506 year 3,000-5,000 fishermen perish on the lake due to nightly storms (Red Cross, 2014).  
507 In the Lake Victoria basin, the diurnal cycle of convection is strongly influenced by  
508 lake/land breezes driven by the thermal gradient between the lake surface and the

509 surrounding land. As the land warms during the course of the day, a lake breeze is  
510 generated which flows from the relatively cooler water towards the warmer land surface.  
511 The circulation is effectively reversed at night, when the land surface becomes cooler  
512 than the lake surface, leading to convergence over the lake and associated thermal  
513 instability.

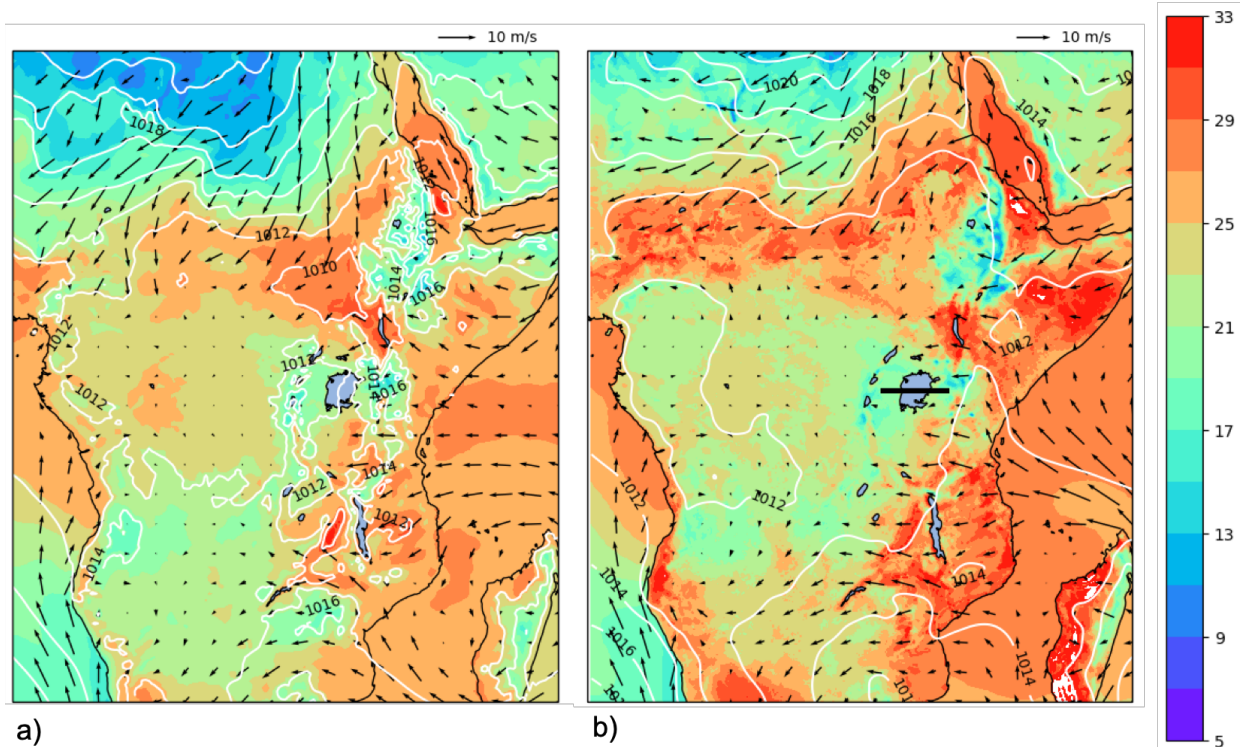
514 In the LKV region, prevailing winds are generally easterly most of the year with some  
515 variability due to the movement of the ITCZ. The local diurnal circulation created by the  
516 presence of the lake within the larger scale easterly wind field creates two diurnal rainfall  
517 maxima. During daylight hours, when the lake breeze begins to advance inland,  
518 convergence is maximized on the eastern coast of the lake as the lake breeze interacts  
519 with the prevailing easterlies. Studies have also noted the importance of downslope  
520 katabatic winds along the mountains to the east of the lake in facilitating convergence  
521 along the eastern coastal regions (Anyah et al. 2006). This creates a maximum in rainfall  
522 and convection on the eastern coast of LKV. Conversely, during nighttime hours, when  
523 the local lake circulation switches to flow from the land towards the lake, the prevailing  
524 easterlies create locally strong easterly flow across the lake and an associated maximum  
525 in convergence and rainfall on the western side of LKV.

526 The LKV simulation starts on 25 November 1999 and extends to the beginning of  
527 December 1999 (Table 2), covering a 5-day period which falls within the short-rain season  
528 of East Africa. The choice of 1999, an ENSO neutral year, was made in order to focus the  
529 analysis on local effects, such as the diurnal convection cycle in response to the lake/land  
530 breeze, with no influence of anomalous large scale conditions. A 1-dimensional lake  
531 model (Hostetler et al. 1993; Bennington et al. 2014) interactively coupled to RegCM4-  
532 NH was utilized to calculate the lake surface temperature (LST), since lake-atmosphere  
533 coupling has been shown to be important for the LKV (Sun et al. 2015; Song et al. 2004).  
534 This coupled lake model has been already used for other lakes, including Lake Malawi in  
535 southern Africa (Diallo et al. 2018). As with the other experiments, the boundary  
536 conditions are provided by a corresponding 12 km RegCM4 simulation employing the  
537 convection scheme of Tiedtke (1996).

538 At the beginning of the simulation, the LST over the lake is uniformly set to 26C, and is  
539 then allowed to evolve according to the lake-atmosphere coupling. This initial LST value  
540 is based on previous studies. For example, Talling (1969) finds Lake Victoria surface  
541 temperatures ranging from 24.5-26°C during the course of the year. Several studies have  
542 used RCMs to investigate the Lake Victoria climate (Anyah et al., 2006; Anyah and  
543 Semazzi 2009, Sun et al. 2015), and found a significant relationship between lake  
544 temperature and rainfall depending on season. The value of 26°C is typical of the winter  
545 season and was chosen based on preliminary sensitivity tests using different values of  
546 initial temperature ranging from 24°C to 26°C.

547 The synoptic feature favorable for the production of precipitation over the LKV in this  
548 period corresponds to a large area of southeasterly flow from the Indian Ocean (Fig. 8a),  
549 which brings low-level warm moist air into the LKV region facilitating the production of  
550 convective instability and precipitation. This synoptic situation, with a low-level  
551 southeasterly jet off the Indian Ocean, is a common feature associated with high  
552 precipitation in the area (Anyah et al. 2006) is found in ERA5 (Figure 7a).

553



554

555 **Figure 8: Mean sea level pressure (mslp) (white black contour lines), surface**  
556 **temperature (color shading) and 100-m wind direction (black arrows) averaged over**  
557 **the period 25 November 00:00 - 1 December 00:00, of ERA5 reanalysis (a) and**  
558 **RegCM 12km (b). The black line (b) shows the cross-section position represented**  
559 **in Fig. 9**

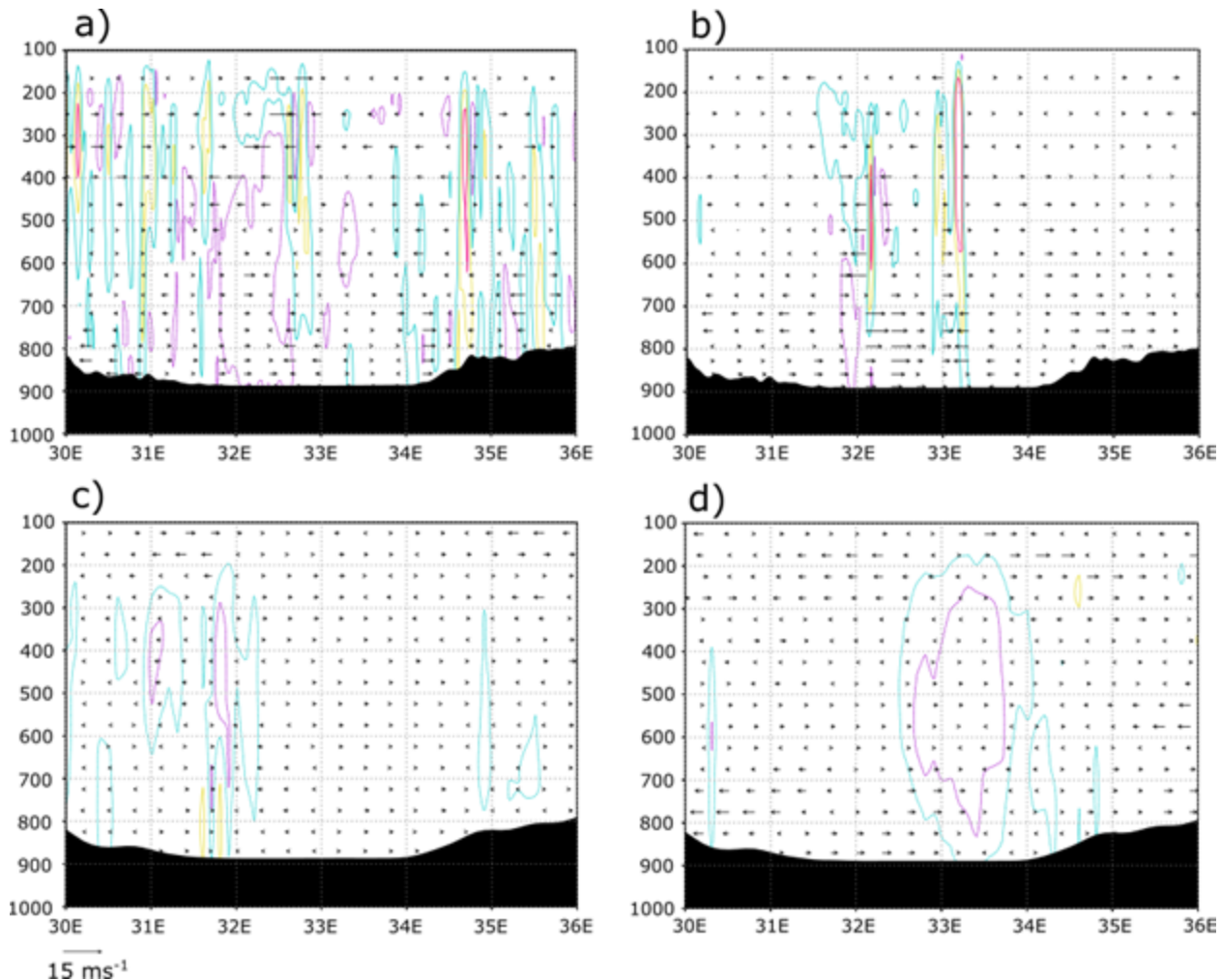
560

561 The LKV region dynamics are quite distinct between nighttime and daytime and the  
562 rainfall in and around the lake has a pronounced diurnal cycle. To understand this strong  
563 diurnal cycle, Figure 9 shows a cross-section through the lake (32E to 34E, black line in  
564 right panel of Fig. 8) along 1S latitude at a period during strong nighttime (Fig. 9b,d; 6Z  
565 30 November) and daytime convection (Fig. 9a,c; 12Z 29 November). During the day,  
566 surface heating around the lake leads to a temperature differential between the land and  
567 lake sufficient to generate a lake breeze, which causes divergence over the lake, while  
568 over the surrounding highlands the environment is more conducive to convection (9a,c).  
569 Conversely, during the night, a land breeze circulation is generated, which induces  
570 convergence and convection over the lake (Figure 9b,d).

571 Comparing the 3 km simulation to the 12 km forcing run, we find that the localized  
572 circulations created by local forcings (i.e. convection) are much stronger in the high  
573 resolution experiment. We also find stronger and more localized areas of convective  
574 updrafts as seen in the vertical velocities (9a,b) compared to the 12 km simulation (8c,d);  
575 omega is shown instead of vertical velocity here because of the difference in model  
576 output). The stronger convection simulated in the 3 km experiment is also tied to the  
577 stronger temperature gradients between lake and land and between day and night (Figure  
578 10).

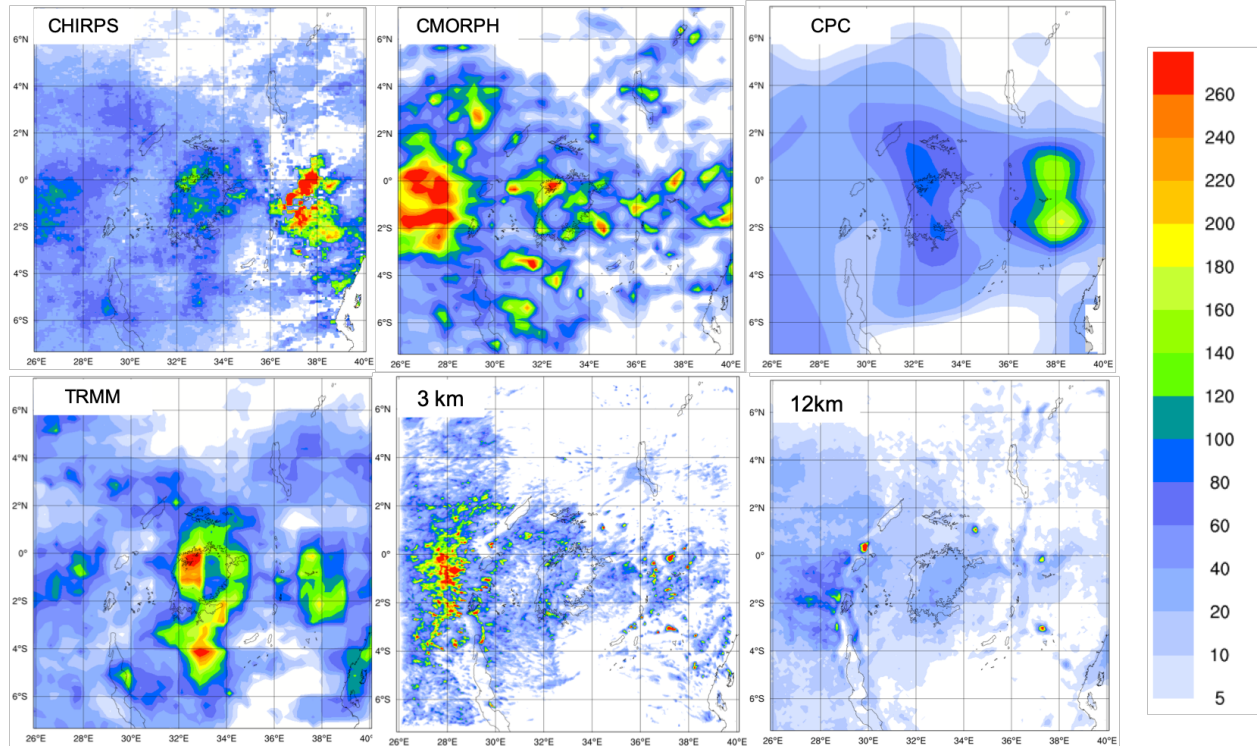
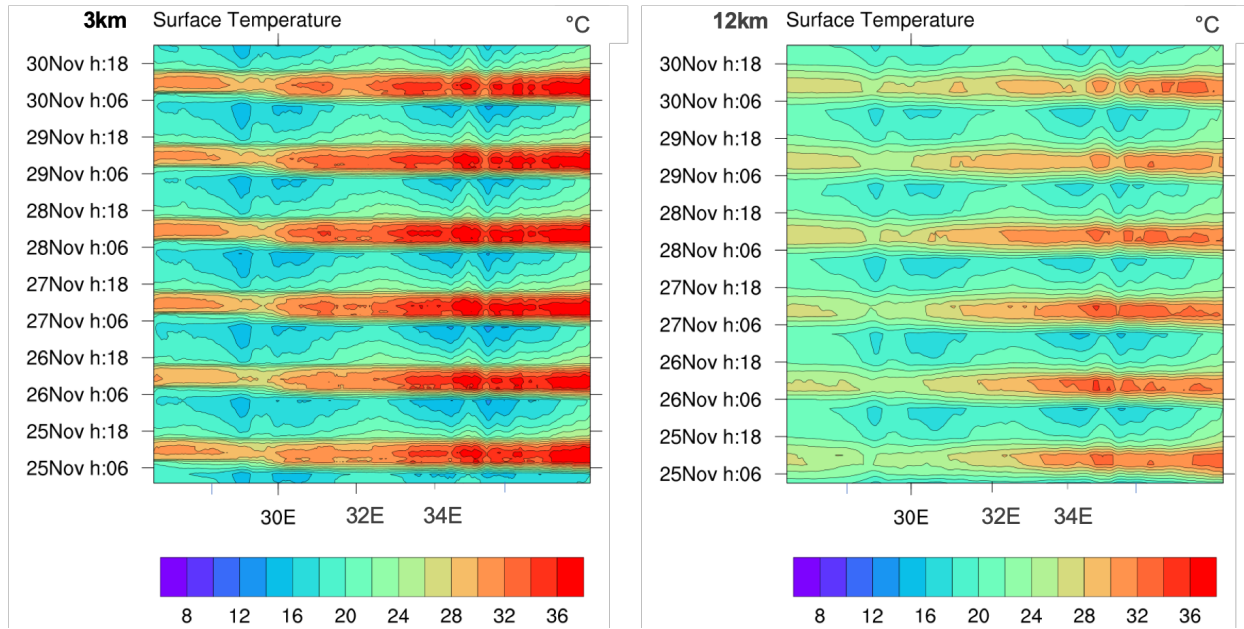
579 This demonstrates that the 3km simulation is better equipped to simulate the localized  
580 circulations associated with this complex land-lake system.

581



582

583 **Figure 9. Cross-section through 1S (red line in bottom right panel of Fig. 9) of the**  
 584 **mean (0-2N) zonal-wind anomaly (30E-36E) vectors and contoured vertical velocity**  
 585 **(m/s) at a) 12Z 29 November and b) 6Z 30 November from the 3km simulation.**  
 586 **Purple dashed contours indicate -0.1 m/s, light blue contours indicate 0.1 m/s,**  
 587 **yellow contours indicate 0.3 m/s, and red contours indicate 0.5 m/s. Lake Victoria**  
 588 **encompasses about 32E to 34E. The bottom 2 panels show the cross-section also**  
 589 **through 1S and mean zonal-wind anomaly vectors as in a) and b) but from the 12km**  
 590 **simulation at c) 12Z 29 November and d) 6Z 30 November. Purple dashed contours**  
 591 **indicate -0.01 hPa/s, light blue dashed contours indicate -0.005 hPa/s, and yellow**  
 592 **dashed contours indicate 0.005 hPa/s.**



598 **Figure 11: Total accumulated precipitation during the LKV case measured by**  
599 **CHIRPS (top left), CMORPH (top center), CPC (top right) TRMM (bottom left) and**  
600 **calculated by RegCM4 at 3 km (bottom center) and 12 km (bottom right) .**

601

602 Figure 11 finally reports the total accumulated precipitation observed and simulated for  
603 the LKV case. TRMM and CPC show a similar pattern, with two-rainfall maxima of  
604 different intensities over the southeastern and northwestern lake areas. CMORPH shows  
605 a western rainfall maximum similar to TRMM and one large rainfall area almost entirely  
606 centered over the highlands to the west of the lake. Conversely in CHIRPS a maximum  
607 is found to the east of the lake while several localized maxima occur over the lake. The  
608 differences between the observed datasets highlight the issue of observational  
609 uncertainty and the need to take into consideration shortcomings associated with the  
610 types of observational datasets considered. Different datasets can have significantly  
611 different climatology, especially in areas of low data availability. For example, Prein and  
612 Gobiet (2017) analyzed two gauge-based European-wide datasets, and seven global low-  
613 resolution datasets, and found large differences across the observation products, often  
614 of similar magnitude as the difference between model simulations. In this case and for  
615 this area the observation uncertainty plays a big role especially at high resolution, and  
616 highlights the need for an adequate observational network for model validation.

617 However, even taking into account the elevated uncertainty existing in the observations  
618 datasets, we find a significant underestimation of rain amounts in the 12 km run (Fig 11),  
619 with a wide area of rainfall around 80mm over the whole of LKV. In contrast, the 3 km  
620 simulation shows substantially greater detail, with rainfall patterns more in agreement with  
621 the CMORPH observations. In particular, the 3 km simulation reproduces well the local  
622 rainfall maxima on the western side of the lake, although these appear more localized  
623 and with a multi-cell structure compared to CMORPH and TRMM. Additionally, the 12 km  
624 simulation underestimates the observed heavy rainfall totals in the highlands to the west  
625 of the lake region, which are instead reproduced by the 3 km simulation.

626 This last test case demonstrates the ability of RegCM4-NH in simulating realistic  
627 convective activity over a morphologically complex region, which is a significant  
628 improvement compared to the hydrostatic-coarse resolution model configuration.

629

### 630 **Conclusions and future outlook**

631

632 In this paper we have described the development of RegCM4-NH, a non hydrostatic  
633 version of the regional model system RegCM4, which was completed in response to the  
634 need of moving to simulations at convection-permitting resolutions of a few km. The  
635 dynamical core of the non-hydrostatic version of MM5 has been thus incorporated into  
636 the RegCM4 system, an approach facilitated by the fact that the this last is essentially an  
637 evolution of the MM5. Some modifications to the MM5 dynamical core were also  
638 implemented to increase the model stability for long term runs. RegCM4-NH also includes  
639 two explicit cloud microphysics schemes needed to explicitly describe convection and  
640 cloud processes in the absence of the use of cumulus convection schemes. Finally, we  
641 presented a few case studies of explosive convection to illustrate how the model provides  
642 realistic results in different settings and general improvements compared to the coarser  
643 resolution hydrostatic version of RegCM4 for such types of events.

644

645 As already mentioned, RegCM4-NH is currently being used for different projects, and  
646 within these contests, is being run at grid spacings of a few km for continuous decadal  
647 simulations, driven by reanalyses of observations or GCM boundary conditions (with the  
648 use of an intermediate resolution domains) over different regions, such as the Alps, the  
649 Eastern Mediterranean, Central-Eastern Europe and the Caribbeans. These projects,  
650 involving multi-model intercomparisons, indicate that the performance of RegCM4-NH is  
651 generally in line with that of other convection permitting models, and exhibits similar  
652 improvements compared to coarser resolution models, such as a better simulation of the  
653 precipitation diurnal cycle and of extremes at hourly to daily time scales. The results  
654 obtained within the multi-model context confirm previous results from single-model  
655 studies (Kendon et al. 2012, 2017, Ban et al. 2014, 2015; Prein et al. 2015, 2017), but

656 also strengthen the robustness of the findings through reduced uncertainty compared to  
657 coarse resolution counterpart (Ban et al., 2021, Pichelli et al., 2021). The convection-  
658 permitting scale can thus open the perspective of more robust projections of future  
659 changes of precipitation, especially over short time scales.

660

661 One of the problems of the RegCM4-NH dynamical core is that, especially for long runs  
662 with varied meteorological conditions, a relatively short time step needs to be used for  
663 stability reasons. This makes the model rather computationally demanding, although not  
664 more than other convection-permitting modeling systems such as the Weather Research  
665 and Forecast model (WRF, Skamarok et al. 2008). For this reason, we are currently  
666 incorporating within the RegCM system a very different and more computationally efficient  
667 non-hydrostatic dynamical core, which will provide the basis for the next version of the  
668 model, RegCM5, to be released in the future.

669

670 Following the philosophy of the RegCM modeling system, RegCM4-NH is intended to be  
671 a public, free, open source community resource for external model users. The non-  
672 hydrostatic dynamical core has been implemented in a way that it can be activated in  
673 place of the hydrostatic dynamics through a user-set switch, which makes the use of  
674 RegCM4-NH particularly simple and flexible. We therefore envision that the model will be  
675 increasingly used by a broad community so that a better understanding can be achieved  
676 of its behavior, advantages and limitations.

677

678 **Code availability:** <https://zenodo.org/record/4603556>

679 **Cases study configuration files:** <https://zenodo.org/record/5106399>

680

681 **Author contribution:** CE prepared the manuscript with contributions from all co-authors  
682 and coordinated research, SP, TA, GR carried out and analysed the simulations, PE  
683 investigated solutions to stabilize/adapt the model at the km-scale and performed  
684 preliminary validation tests, GG developed/adapted the model code, FDS contributed to  
685 develop the coupled version of the model, NR developed one of the microphysics  
686 scheme, GF supervised and coordinated all activities.

687

688 **Competing interests:** The authors declare that they have no conflict of interest.

689

690

691 **References**

692 Anyah, R., Semazzi, F. H. M., Xie, L., 2006: Simulated Physical Mechanisms Associated  
693 with Climate Variability over Lake Victoria Basin in East Africa, *Mon. Wea. Rev.*, 134  
694 3588-3609.

695

696 Anthes, R. A., Hsie, E. -Y., & Kuo, Y. -H. (1987). Description of the Penn State/NCAR  
697 Mesoscale Model: Version 4 (MM4) (No. NCAR/TN-282+STR). doi:10.5065/D64B2Z90

698

699 Anyah, R. O., F. H. M. Semazzi, L. Xie, 2006: Simulated Physical Mechanisms  
700 Associated with Climate Variability over Lake Victoria Basin in East Africa. *Mon. Wea.*  
701 *Rev.*, 134, 3588-3609.,

702

703 Anyah RO, Semazzi F (2009) Idealized simulation of hydrodynamic characteristics of  
704 Lake Victoria that potentially modulate regional climate. *Int J Climatol* 29(7):971–981.  
705 doi:10.1002/joc.1795

706

707 Ashouri, Hamed, Kuo Lin Hsu, Soroosh Sorooshian, Dan K. Braithwaite, Kenneth R.  
708 Knapp, L. Dewayne Cecil, Brian R. Nelson and Olivier P. Prat (2015). 'PERSIANN- CDR:  
709 Daily precipitation climate data record from multisatellite observations for hydrological and  
710 climate studies'. In: *Bulletin of the American Meteorological Society*. ISSN: 00030007.  
711 DOI: 10.1175/BAMS-D-13-00068.1.

712

713 Ban, N., J. Schmidli, and C. Schär, 2014: Evaluation of the convection-resolving regional  
714 climate modeling approach in decade-long simulations. *J. Geophys. Res. Atmos.*, 119,  
715 7889– 7907, <https://doi.org/10.1002/2014JD021478>.

716

717 Ban N, Schmidli J, Schär C (2015) Heavy precipitation in a changing climate: does short-  
718 term summer precipitation increase faster? *Geophys Res Lett* 42:1165–1172.  
719 <https://doi.org/10.1002/2014GL062588>

720 Ban, N., Caillaud, C., Coppola, E. *et al.* The first multi-model ensemble of regional climate  
721 simulations at kilometer-scale resolution, part I: evaluation of precipitation. *Clim Dyn*  
722 (2021). <https://doi.org/10.1007/s00382-021-05708-w>

723

724 Beheng, K.: A parameterization of warm cloud microphysical conversion processes,  
725 *Atmos. Res.*, 33, 193–206, 1994

726

727 Bennington V, Notaro M, Holman KD, 2014: Improving Climate Sensitivity of Deep Lakes  
728 within a Regional Climate Model and Its Impact on Simulated Climate, *J. Clim*, 27, 2886–  
729 2911.

730

731 Bretherton CS, McCaa JR, Grenier H (2004) A new parameterization for shallow cumulus  
732 convection and its application to marine subtropical cloud-topped boundary layers. I.  
733 Description and 1D results. *Mon Weather Rev* 132: 864– 882

734

735 Chan, S. C., E. J. Kendon, H. J. Fowler, S. Blenkinsop, N. M. Roberts, and C. A. T. Ferro,  
736 2014: The value of high- resolution Met Office regional climate models in the simula-  
737 tion of multi-hourly precipitation extremes. *J. Climate*, 27, 6155–6174,  
738 <https://doi.org/10.1175/JCLI-D-13-00723.1>.

739

740 Chen, Mingyue and Pingping Xie (2008). ‘CPC Unified Gauge-based Analysis of Global  
741 Daily Precipitation’. In: 2008 Western Pacific Geophysics Meeting. ISBN: 0026- 0576.  
742 DOI: [http://dx.doi.org/10.1016/S0026-0576\(07\)80022-5](http://dx.doi.org/10.1016/S0026-0576(07)80022-5).

743

744

745 Clark, P., N. Roberts, H. Lean, S. P. Ballard, and C. Charlton- Perez, 2016: Convection-  
746 permitting models: A step-change in rainfall forecasting. *Meteor. Appl.*, 23, 165–181,  
747 <https://doi.org/10.1002/met.1538>.

748

749 Coppola, E., Sobolowski, S., Pichelli, E. et al. A first-of-its-kind multi-model convection  
750 permitting ensemble for investigating convective phenomena over Europe and the  
751 Mediterranean. *Clim Dyn* 55, 3–34 (2020). <https://doi.org/10.1007/s00382-018-4521-8>

752

753 Coppola E, Giorgi F, Mariotti L, Bi X (2012) RegT-Band: a tropical band version of  
754 RegCM4. *Clim Res* 52: 115–133

755

756 Dacre, H. F., P. A. Clark, O. Martinez-Alvarado, M. A. Stringer, and D. A. Lavers, 2015:  
757 How do atmospheric rivers form? *Bull. Amer. Meteor. Soc.*, 96, 1243-1255,  
758 <https://doi.org/10.1175/BAMS-D-14-00031>.

759 Dale, M., A. Hosking, E. Gill, E. J. Kendon, H. J. Fowler, S. Blenkinsop, and S. C. Chan,  
760 2018: Understanding how changing rainfall may impact on urban drainage systems; les-  
761 sons from projects in the UK and USA. *Water Pract. Technol.*, 13, 654–661,  
762 <https://doi.org/10.2166/wpt.2018.069>.

763

764 Diallo, I., Giorgi, F. and Stordal, F. (2018) Influence of Lake Malawi on regional climate  
765 from a double nested regional climate model experiment. *Climate Dynamics*, 50, 3397–  
766 3411. <https://doi.org/10.1007/s00382-017-3811-x>

767

768 Dickinson, R.E., Errico, R.M., Giorgi, F. et al. A regional climate model for the western  
769 United States. *Climatic Change* 15, 383–422 (1989). <https://doi.org/10.1007/BF00240465>

770

771 Dickinson RE, Henderson-Sellers A, Kennedy P (1993) Bio -sphere– atmosphere transfer  
772 scheme (BATS) version 1eas coupled to the NCAR community climate model. *TechRep*,  
773 National Center for Atmospheric Research TechNote NCAR.TN-387+ STR, NCAR,  
774 Boulder, CO

775

776 Done, J., C. A. Davis, and M. L. Weisman, 2004: The next generation of NWP: Explicit  
777 forecasts of convection using the Weather Research and Forecasting (WRF) model.  
778 *Atmos. Sci. Lett.*, 5, 110–117, <https://doi.org/10.1002/asl.72>.

779

780 DUDHIA, J., 1989: Numerical study of convection observed during the winter monsoon  
781 experiment using a mesoscale two-dimensional model, *J. Atmos. Sci.*, 46, 3077–3107.

782

783 Durran D.R. and Klemp J.B.: A compressible model for the simulation of moist mountain  
784 waves, *Mon. Wea. Rev.*, 111, 2341–236, 1983.

785

786 Elguindi N., Bi X., Giorgi F. , Nagarajan, B. Pal J., Solmon F., Rauscher S., Zakey S.,  
787 O'Brien T., Nogherotto R. and Giuliani G., 2017: Regional Climate Model  
788 RegCMReference ManualVersion 4.7, 49 pp, <https://zenodo.org/record/4603616>

789

790 Emanuel KA (1991) A scheme for representing cumulus convection in large-scale  
791 models. *J Atmos Sci* 48:2313–2335

792

793 Fairall, C.W., E.F. Bradley, J.S. Godfrey, G.A. Wick, J.B. Edson, and G.S. Young, 1996a:  
794 The cool skin and the warm layer in bulk flux calculations. *J. Geophys. Res.* 101, 1295–  
795 1308.

796

797 Fairall, C.W., E.F. Bradley, D.P. Rogers, J.B. Edson, G.S. Young, 1996b: Bulk  
798 parameterization of air-sea fluxes for TOGA COARE. *J. Geophys. Res.* 101, 3747-3764

799

800 Funk, C., Peterson, P., Landsfeld, M. et al. The climate hazards infrared precipitation with  
801 stations—a new environmental record for monitoring extremes. *Sci Data* 2, 150066  
802 (2015). <https://doi.org/10.1038/sdata.2015.66>

803

804 Gimeno, L., R. Nieto, M. Vásquez, and D. A. Lavers, 2014: Atmospheric rivers: A mini-  
805 review. *Front. Earth Sci.*, 2, <https://doi.org/10.3389/feart.2014.00002>.

806

807 Giorgi F (2019) Thirty years of regional climate modeling: where are we and where are  
808 we going next? *J Geophys Res Atmos* 124:5696–5723

809

810 Giorgi F, Coppola E, Solmon F, Mariotti L and others (2012) RegCM4: model description  
811 and preliminary tests over multiple CORDEX domains. *Clim Res* 52:7-29.  
812 <https://doi.org/10.3354/cr01018>

813

814

815

816 Giorgi F, Francisco R, Pal JS (2003) Effects of a sub-gridscale topography and landuse  
817 scheme on surface climate and hydrology. I. Effects of temperature and water  
818 vapor disaggregation. *J Hydrometeorol* 4: 317– 333

819

820 Giorgi F, Jones C, Asrar G (2009) Addressing climate information needs at the regional  
821 level: the CORDEX framework. *WMO Bull* 175–183

822

823 Giorgi F, Mearns LO (1999) Introduction to special section: regional climate modeling  
824 revisited. *J Geophys Res* 104:6335–6352

825

826 Giorgi F, Marinucci MR, Bates G (1993a) Development of a second generation regional  
827 climate model (RegCM2). I. Boundary layer and radiative transfer processes.  
828 *Mon Weather Rev* 121: 2794–2813

829

830 Giorgi F, Marinucci MR, Bates G, DeCanio G (1993b) Development of a second  
831 generation regional climate model (RegCM2), part II: convective processes and  
832 assimilation of lateral boundary conditions. *Mon Weather Rev* 121:2814–2832

833

834 Giorgi, F., and G. T. Bates, 1989: The Climatological Skill of a Regional Model over  
835 Complex Terrain. *Mon. Wea. Rev.*, 117, 2325–2347, [https://doi.org/10.1175/1520-0493\(1989\)117<2325:TCSOAR>2.0.CO;2](https://doi.org/10.1175/1520-0493(1989)117<2325:TCSOAR>2.0.CO;2).

837 G. A. Grell, J. Dudhia and D. R. Stauffer, "A Description of the Fifth Generation Penn  
838 State/NCAR Mesoscale Model (MM5)," NCAR Tech. Note, NCAR/TN-398+ STR,  
839 Boulder, 1995, p. 122.

840

841 Grell GA (1993) Prognostic evaluation of assumptions used by cumulus  
842 parameterizations. *Mon Weather Rev* 121: 764– 787

843

844 Grell, G., A.J. Dudhia, and D.R. Stauffer, 1994, A description of the fifth-generation Penn  
845 State/NCAR mesoscale model (MM5). NCAR Technical Note, NCAR/TN- 398+STR.

846

847 Gunn, K. L. S., and J. S. Marshall, 1958: The distribution with size of aggregate  
848 snowflakes. *J. Meteor.*, 15, 452–461, [https://doi.org/10.1175/1520-0469\(1958\)015<0452:TDWSOA>2.0.CO;2](https://doi.org/10.1175/1520-0469(1958)015<0452:TDWSOA>2.0.CO;2).

849

850

851 Gutowski Jr., W. J., Giorgi, F., Timbal, B., Frigon, A., Jacob, D., Kang, H.-S., Raghavan,  
852 K., Lee, B., Lennard, C., Nikulin, G., O'Rourke, E., Rixen, M., Solman, S., Stephenson,  
853 T., and Tangang, F.: WCRP COordinated Regional Downscaling EXperiment (CORDEX):  
854 a diagnostic MIP for CMIP6, *Geosci. Model Dev.*, 9, 4087–4095,  
855 <https://doi.org/10.5194/gmd-9-4087-2016>, 2016

856

857 Holtslag A, de Bruijn E, Pan HL (1990) A high resolution air mass transformation model  
858 for short-range weather fore-casting. *Mon Weather Rev* 118: 1561–1575

859

860 Hostetler SW, Bates GT, Giorgi F (1993) Interactive nesting of a lake thermal model within  
861 a regional climate model for climate change studies. *J Geophys Res* 98: 5045– 5057

862

863 Huffman, G. J., and Coauthors, 2007: The TRMM Multisatellite Precipitation Analysis  
864 (TMPA): Quasi-global, multiyear, combined-sensor precipitation estimates at fine scales.  
865 *J. Hydrometeor.*, 8, 38–55, doi:<https://doi.org/10.1175/JHM560.1>

866

867 Kiehl J, Hack J, Bonan G, Boville B, Breigleb B, WilliamsonD, Rasch P (1996) Description  
868 of the NCAR Commun -ity Climate Model (CCM3). National Center for Atmo spheric  
869 Research Tech Note NCAR/TN-420+ STR, NCAR,Boulder, CO  
870

871 Lean, H. W., P. A. Clark, M. Dixon, N. M. Roberts, A. Fitch, R. Forbes, and C. Halliwell,  
872 2008: Characteristics of high- resolution versions of the Met Office Unified Model for  
873 forecasting convection over the United Kingdom. *Mon. Wea. Rev.*, 136, 3408–3424,  
874 <https://doi.org/10.1175/2008MWR2332.1>.

875

876 Lind, P., D. Lindstedt, E. Kjellstrom, and C. Jones, 2016: Spatial and temporal  
877 characteristics of summer precipitation over central Europe in a suite of high-resolution  
878 climate models. *J. Climate*, 29, 3501–3518, <https://doi.org/10.1175/JCLI-D-15- 0463.1>.

879

880 Hewitt, C. D., and J. A. Lowe, 2018: Toward a European climate prediction system. *Bull.*  
881 *Amer. Meteor. Soc.*, 99, 1997–2001, <https://doi.org/10.1175/BAMS-D-18-0022.1>.

882 Hong, S.-Y., H.-M. H. Juang, and Q. Zhao, 1998: Implementation of prognostic cloud  
883 scheme for a regional spectral model, *Mon. Wea. Rev.*, 126, 2621–2639.

884

885 Hong, S.-Y., J. Dudhia, and S.-H. Chen, 2004: A Revised Approach to Ice Microphysical  
886 Processes for the Bulk Parameterization of Clouds and Precipitation, *Mon. Wea. Rev.*,  
887 132, 103–120.

888

889 Hong, S.-Y., and J.-O. J. Lim, 2006: The WRF Single-Moment 6-Class Microphysics  
890 Scheme (WSM6), *J. Korean Meteor. Soc.*, 42, 129–151

891

892 Hostetler SW, Bates GT, Giorgi F, 1993: Interactive Coupling of Lake Thermal Model with  
893 a Regional climate Model, *J. Geophys. Res.*, 98(D3), 5045-5057.

894

895 Huffman, George J., David T. Bolvin, Eric J. Nelkin, David B. Wolff, Robert F. Adler,  
896 Guojun Gu, Yang Hong, Kenneth P. Bowman and Erich F. Stocker (2007). The TRMM

897 Multisatellite Precipitation Analysis (TMPA): Quasi-Global, Multiyear, Combined-Sensor  
898 Precipitation Estimates at Fine Scales. DOI: 10.1175/JHM560.1.

899

900 Joyce, Robert J., John E. Janowiak, Phillip A. Arkin, Pingping Xie, 2004: CMORPH: A  
901 Method that Produces Global Precipitation Estimates from Passive Microwave and  
902 Infrared Data at High Spatial and Temporal Resolution. *J. Hydrometeor*, 5, 487–503

903

904 Kain, J. S., 2004: The Kain–Fritsch convective parameterization: An update. *J. Appl.*  
905 *Meteor.*, 43, 170–181, [https://doi.org/10.1175/1520-0450\(2004\)043<0170:TKCPAU>2.0.CO;2](https://doi.org/10.1175/1520-0450(2004)043<0170:TKCPAU>2.0.CO;2).

907

908 Kain, J. S., and J. M. Fritsch, 1990: A one-dimensional entraining/ detraining plume model  
909 and its application in convective parameterization, *J. Atmos. Sci.*, 47, 2784–2802.

910

911 Kendon, E. J., N. M. Roberts, C. A. Senior, and M. J. Roberts, 2012: Realism of rainfall  
912 in a very high-resolution regional climate model. *J. Climate*, 25, 5791–5806,  
913 <https://doi.org/10.1175/JCLI-D-11-00562.1>.

914

915 Kendon, E. J., and Coauthors, 2017: Do convection-permitting regional climate models  
916 improve projections of future precipitation change? *Bull. Amer. Meteor. Soc.*, 98, 79–93,  
917 <https://doi.org/10.1175/BAMS-D-15-0004.1>

918

919 Kessler, E., 1969: On the Distribution and Continuity of Water Substance in Atmospheric  
920 Circulations. *Meteor. Monogr.*, No. 32, Amer. Meteor. Soc., 84 pp.

921

922 Khairoutdinov, M. and Kogan, Y.: A new cloud physics parameterization in a large-eddy  
923 simulation model of marine stratocumulus, *B. Am. Meteorol. Soc.*, 128, 229–243, 2000

924

925 Klemp, J.B. and Dudhia, J.: An Upper Gravity-Wave Absorbing Layer for NWP  
926 Applications, *Monthly Weather Review*, 176, 3987–4004, 2008.

927

928 Klemp, J. B. and D. K. Lilly: Numerical simulation of hydrostatic mountain waves, *J.*  
929 *Atmos. Sci.*, 35, 78–107, 1978.

930

931 Lin, Y., Farley, R., and Orville, H.: Bulk parameterization of the snow field in a cloud  
932 model, *J. Appl. Meteor. Clim.*, 22, 1065–1092, 1983.

933

934 Marshall, J. S., and W. McK. Palmer, 1948: The distribution of raindrops with size. *J.*  
935 *Meteor.*, 5, 165–166.

936

937 Matte, Dominic; Laprise, René; Thériault, Julie M.; Lucas-Picher, Philippe (2017). Spatial  
938 spin-up of fine scales in a regional climate model simulation driven by low-resolution  
939 boundary conditions. *Climate Dynamics*, 49(1-2), 563–574. doi:10.1007/s00382-016-  
940 3358-2

941

942 Mlawer, E. J., S. J. Taubman, P. D. Brown, M. J. Iacono, and S. A. Clough, 1997:  
943 Radiative transfer for inhomogeneous atmospheres: RRTM, a validated correlated-k  
944 model for the longwave. *J. Geophys. Res.*, 102, 16,663-16,682

945

946 Nogherotto, R., Tompkins, A.M., Giuliani, G., Coppola, E. and Giorgi, F.: Numerical  
947 framework and performance of the new multiple-phase cloud microphysics scheme in  
948 RegCM4. 5: precipitation, cloud microphysics, and cloud radiative effects. *Geoscientific*  
949 *Model Development*, 9(7), 2533-2547, 2016

950

951 Oleson, K. W., Lawrence, D. M., Bonan, G. B., Drewniak, B., Huang, M., Koven, C. D.,  
952 Levis, S., Li, F., Riley, W. J., Subin, Z. M., Swenson, S. C., Thornton, P. E., Bozbiyik, A.,  
953 Fisher, R., Kluzeck, E., Lamarque, J. -F., Lawrence, P. J., Leung, L. R., Lipscomb, W.,  
954 Muszala, S., Ricciuto, D. M., Sacks, W., Sun, Y., Tang, J., and Yang, Z. -L:Technical  
955 Description of version 4.5 of the Community Land Model (CLM),Ncar Technical Note  
956 NCAR/TN-503+STR, National Center for Atmospheric Research, Boulder, CO, 422 pp,  
957 DOI: 10.5065/D6RR1W7M, 2013.

958

959 Pal JS, Small E, Eltahir E (2000) Simulation of regional-scale water and energy budgets:  
960 representation of subgrid cloud and precipitation processes within RegCM. *J Geo-phys*  
961 *Res* 105: 29579–29594

962

963 Pal JS et al (2007) The ICTP RegCM3 and RegCNET: regional climate modeling for the  
964 developing world. *Bull Am Meteorol Soc* 88:1395–1409

965

966 Pichelli, E., Coppola, E., Sobolowski, S. et al. The first multi-model ensemble of regional  
967 climate simulations at kilometer-scale resolution part 2: historical and future simulations  
968 of precipitation. *Clim Dyn* (2021). <https://doi.org/10.1007/s00382-021-05657-4>

969

970 Prein, Andreas F. and Andreas Gobiet (2017). ‘Impacts of uncertainties in European  
971 gridded precipitation observations on regional climate analysis’. In: *International Journal*  
972 of *Climatology*. ISSN: 10970088. DOI: 10.1002/joc.4706

973

974 Prein, A. F. et al. A review on regional convection-permitting climate modeling:  
975 demonstrations, prospects, and challenges. *Rev. Geophys.* 53, 323–361 (2015).

976

977 Ralph, F. M., P. J. Neiman, G. A. Wick, S. I. Gutman, M. D. Dettinger, D. R. Cayan, and A.  
978 B. White, 2006: Flooding on California’s Russian River: Role of atmospheric rivers.  
979 *Geophys. Res. Lett.*, 33, L13801, <https://doi.org/10.1029/2006GL026689>

980

981 Ralph, F. M., M. D. Dettinger, M. M. Cairns, T. J. Galarneau, and J. Eylander, 2018:  
982 Defining “atmospheric river”: How the Glossary of Meteorology helped resolve a debate.  
983 *Bull. Amer. Meteor. Soc.*, 99, 837–839, <https://doi.org/10.1175/BAMS-D-17-0157.1>

984

985 Rutledge, S. A., and P. V. Hobbs, 1983: The mesoscale and microscale structure and  
986 organization of clouds and precipitation in midlatitude cyclones. Part VIII: A model for the  
987 “seeder-feeder” process in warm-frontal rainbands. *J. Atmos. Sci.*, 40, 1185–1206.

988

989 Skamarock WC, Klemp JB, Dudhia J, Gill DO, Barker DM, Duda MG, Huang XY, Wang  
990 W, Powers JG. 2008. 'A description of the advanced research WRF version 3', Technical  
991 Note NCAR/TN-475+STR. NCAR: Boulder, CO  
992  
993 Schwartz, C. S., 2014: Reproducing the September 2013 record- breaking rainfall over  
994 the Colorado Front Range with high- resolution WRF forecasts. *Wea. Forecasting*, 29,  
995 393–402, <https://doi.org/10.1175/WAF-D-13-00136.1>  
996  
997 Sitz, L. E., F. Sante, R. Farneti, R. Fuentes-Franco, E. Coppola, L. Mariotti, M. Reale, et  
998 al. 2017. "Description and Evaluation of the Earth System Regional Climate Model  
999 (RegCM-ES)." *Journal of Advances in Modeling Earth Systems*.  
1000 doi:10.1002/2017MS000933  
1001  
1002 Song Y, Semazzi HMF, Xie L, Ogallo LJ, 2004: A coupled regional climate model for the  
1003 Lake Victoria Basin of East Africa. *Int. J. Climatol.* 24: 57-75.  
1004  
1005 Sun X, Xie L, Semazzi F, Liu B, 2015: Effect of Lake Surface Temperature on the Spatial  
1006 Distribution and Intensity of the Precipitation over the Lake Victoria Basin. *Mon. Wea.  
1007 Rev.* 143: 1179-1192.  
1008  
1009 Sundqvist, H., Berge, E., and Kristjansson, J.: Condensation and cloud parameterization  
1010 studies with a mesoscale numerical weather prediction model, *Mon. Weather Rev.*, 117,  
1011 1641–1657, 1989.  
1012  
1013 Talling, J. F. (1969) The incidence of vertical mixing, and some biological and chemical  
1014 consequences, in tropical African lakes, *Verh. Int. Ver. Limnol.* 17, 998-1012 DOI:  
1015 10.1080/03680770.1968.11895946  
1016  
1017 Tiedtke, M., 1989, A comprehensive mass flux scheme for cumulus parametrization in  
1018 large-scale models. *Mon. Weather Rev.*, 117, 1779–1800  
1019

1020 Tiedtke, M., 1993: Representation of Clouds in Large-Scale Models. *Mon. Wea. Rev.*,  
1021 121, 3040–3061, [https://doi.org/10.1175/1520-0493\(1993\)121<3040:ROCILS>2.0.CO;2](https://doi.org/10.1175/1520-0493(1993)121<3040:ROCILS>2.0.CO;2)

1022

1023 Tiedtke, M., . 1996: An extension of cloud-radiation parameterization in the ECMWF  
1024 model: The representation of subgrid-scale variations of optical depth. *Mon. Wea. Rev.*,  
1025 124, 745–750

1026

1027 Tompkins, A.: Ice supersaturation in the ECMWF integrated fore-*cast* system, *Q. J. Roy.*  
1028 *Meteor. Soc.*, 133, 53–63, 2007

1029

1030 Tripoli, G. J., and W. R. Cotton, 1980: A numerical investigation of several factors  
1031 contributing to the observed variable intensity of deep convection over south Florida. *J.*  
1032 *Appl. Meteor.*, 19, 1037–1063.

1033

1034 Williams PD. 2009. A proposed modification to the Robert–Asselin time filter. *Mon.*  
1035 *Weather Rev.* 137: 2538–2546

1036

1037 Weisman, M. L., C. Davis, W. Wang, K. W. Manning, and J. B. Klemp, 2008: Experiences  
1038 with 0–36-h explicit convective forecasts with the WRF-ARW model. *Wea. Forecasting*,  
1039 23, 407–437, <https://doi.org/10.1175/2007WAF2007005.1>

1040

1041 Weusthoff, T., F. Ament, M. Arpagaus, and M. W. Rotach, 2010: Assessing the benefits  
1042 of convection-permitting models by neighbor hood verification: Examples from MAP D-  
1043 PHASE. *Mon. Wea. Rev.*, 138, 3418–3433, <https://doi.org/10.1175/2010MWR3380.1>.

1044

1045 Zeng X, Zhao M, Dickinson RE (1998) Intercomparison of bulk aerodynamic algorithms  
1046 for the computation of seafloor fluxes using TOGA COARE and TAO data. *J Clim* 11:  
1047 2628–2644

1048

1049 Zhu, Y., and R. E. Newell, 1998: A proposed algorithm for moisture fluxes from  
1050 atmospheric rivers. *Mon. Wea. Rev.*, 126, 725–735, [https://doi.org/10.1175/1520-0493\(1998\)126<0725:APAFMF>2.0.CO;2](https://doi.org/10.1175/1520-0493(1998)126<0725:APAFMF>2.0.CO;2).

1052

1053